JCB Journal of Cell Biology

REPORT

Small lipid droplets are rigid enough to indent a nucleus, dilute the lamina, and cause rupture

Irena L. Ivanovska[1*], Michael P. Tobin[1*], Tianyi Bai[1], Lawrence J. Dooling[1], and Dennis E. Discher[1]

The nucleus in many cell types is a stiff organelle, but fat-filled lipid droplets (FDs) in cytoplasm are seen to indent and displace the nucleus. FDs are phase-separated liquids with a poorly understood interfacial tension γ that determines how FDs interact with other organelles. Here, micron-sized FDs remain spherical as they indent peri-nuclear actomyosin and the nucleus, while causing local dilution of Lamin-B1 independent of Lamin-A,C and sometimes triggering nuclear rupture. Focal accumulation of the cytosolic DNA sensor cGAS at the rupture site is accompanied by sustained mislocalization of DNA repair factors to cytoplasm, increased DNA damage, and delayed cell cycle. Macrophages show FDs and engulfed rigid beads cause similar indentation dilution. Spherical shapes of small FDs indicate a high γ, which we measure for FDs mechanically isolated from fresh adipose tissue as ∼40 mN/m. This value is far higher than that of protein condensates, but typical of oils in water and sufficiently rigid to perturb cell structures including nuclei.

Introduction

Many cell types have fat-filled lipid droplets (FDs), including cancer cells and macrophages that acquire fatty acids to make FDs (Cruz et al., 2020; Hill et al., 2018; Su et al., 2020). In some tissue cells such as adipocytes, FDs abut the nucleus (Farese and Walther, 2009), and although fat is soft to the touch, nuclear stiffness and strength are high based on the surprisingly high expression levels of mechanosensitive Lamin-A,C (Swift et al., 2013). The farnesylated lamins B1 and B2 are comparatively constant across tissues including fat, and they prevent nuclear rupture in cells which lack Lamin-A,C such as neurons (Chen et al., 2019) that are susceptible to FD-associated cellular stress (Ralhan et al., 2021). Such observations suggest an overall hypothesis that FDs somehow possess sufficient rigidity to act as intracellular mechanical stressors of organelles including the nucleus. Addressing this hypothesis might eventually clarify, for example, how fat is lost with aging of some stiff tissues such as skin or provide insights into how lipodystrophy is caused by HIV protease inhibitors, farnesylation inhibitors (Anuurad et al., 2010), and mutations that suppress mature Lamin-A (Bidault et al., 2011).

FDs appear fluid in FRAP measurements (Lyu et al., 2021) but have also been assumed to be solid and softer than the nucleus in mesenchymal stem cells (MSCs) during adipogenesis (Shoham et al., 2014). We had noted previously (Swift et al., 2013) and observe again here that micron-sized FDs in MSCs can visibly indent the nucleus (Fig. 1, A i)—despite the fluidity of FDs in freshly isolated fat tissue (Fig. S1 A). FDs are often described as having an interfacial tension γ, or energy per area (units of mN/m), set by their oily triacylglycerols and sterol esters (Hsieh et al., 2012; Murphy and Vance, 1999) and modulated by a surrounding monolayer of ER-derived phospholipid and protein (Farese and Walther, 2009; Thiam et al., 2013). The particular value of γ is important because the pressure (force per area) that an FD exerts against a nucleus is set by γ multiplied by the FDs' curvature (radius^{-1}; Fig. 1, A ii). Furthermore, any distortion from a spherical shape necessarily increases an FDs' surface area and costs an energy set by γ (Fig. 1, A ii, scales). For comparison, protein "condensates" or aggregates have such a low γ of <1 k_BT/(10 nm^2) that they can be highly elongated to non-spherical shapes merely by cytoskeleton interactions (Böddeker et al., 2022).

The crescent shape of a nucleus at the periphery of a mature adipocyte that has just one giant FD filling the cytoplasm (Fig. 1, A iii) seems consistent with electron microscopy images that also suggest indentation (Verstraeten et al., 2011). However, whether FDs are sufficiently rigid to indent a nucleus and perturb key functions such as DNA repair and replication remains unclear. It is generally important because—even for nonmigratory adipocytes—nuclear rupture in interphase is possible (De Vos et al., 2011; Nmezi et al., 2019; Tamiello et al., 2013), and associates somehow with high nuclear curvature and DNA damage (Cho et al., 2019; Pfeifer et al., 2018; Xia et al., 2018). In

[1]Molecular and Cell Biophysics Lab, University of Pennsylvania, Philadelphia, PA, USA.

*I.L. Ivanovska and M.P. Tobin contributed equally to this paper. Correspondence to Dennis E. Discher: discher@seas.upenn.edu.

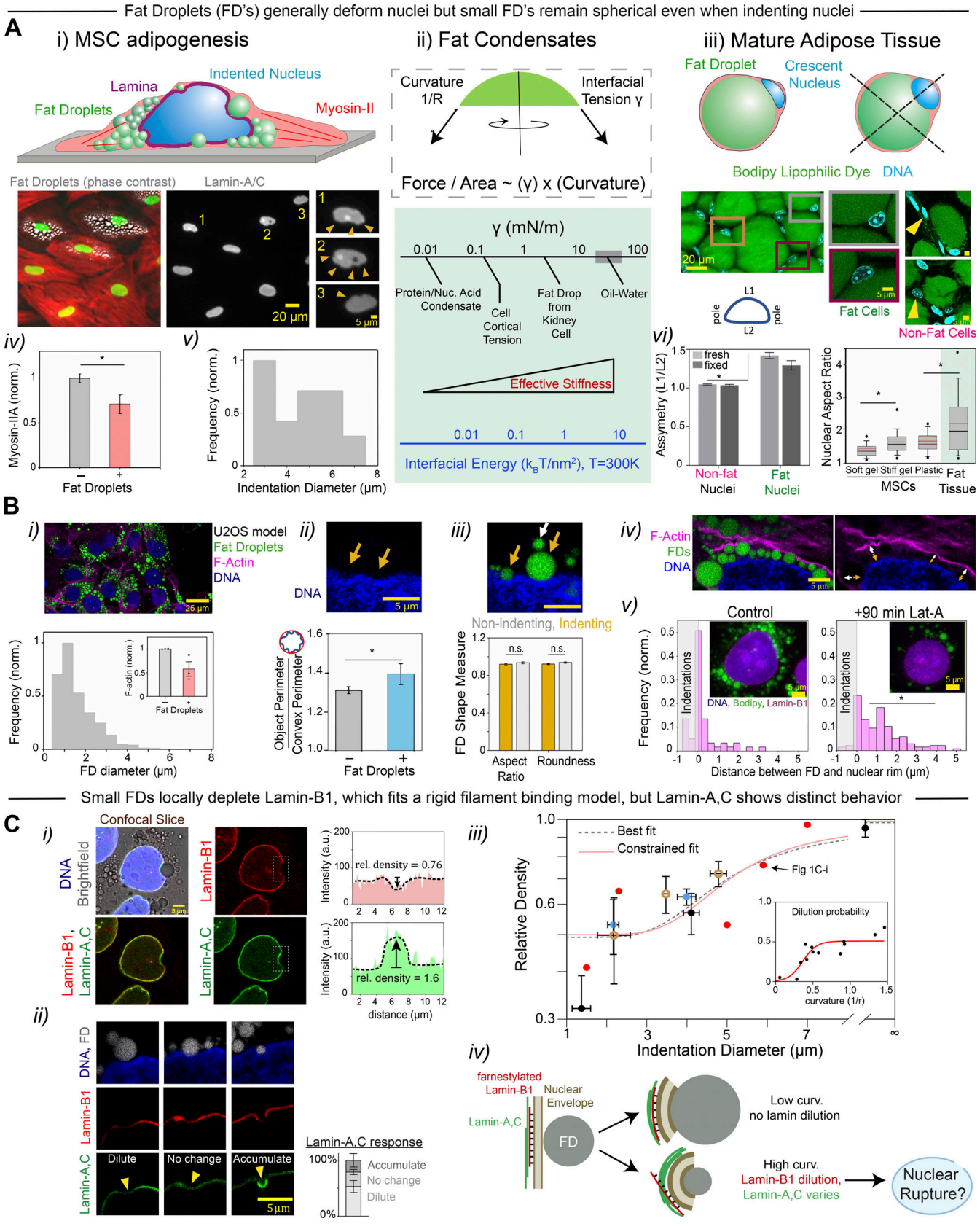

Figure 1. **FDs of varying size deform the nucleus and alter nuclear lamina density at indentation sites of high Gaussian curvature. (A i)** Adherent cell in culture filled with FDs illustrates possible indentation of the nucleus. MSCs treated with adipogenic induction media for ~2 wk show such indentations in fixed and immunostained samples (arrowheads). **(A ii)** The pressure (force per area) needed for deformation of an FD and nucleus is the product of interfacial tension

(γ) and Gaussian curvature, with large (low curvature) FDs deforming at lower stress. A high γ relative to other cell tensions is anticipated for FDs and is currently known only for FDs from sonicated lysates of kidney cells (Cos7 and HEK) and fly hemocyte-like embryonic cells, with γ = 2–5 mN/m for ∼3–10-µm-diam FDs (Ben M'barek et al., 2017; Lyu et al., 2021). **(A iii)** Representative images show cells in fat tissue harbor large FDs that squeeze the nucleus to the cell periphery and flatten it, whereas nuclei in non-fat cells have axisymmetric shapes (arrowheads). **(A iv and v)** Actomyosin is suppressed in MSCs with FDs, and nuclear indentation caused by FDs varies within the micron range (error bars are means ± SEM, n = 20 cells, representative of duplicate experiments, *, P < 0.05, significance is determined by Mann–Whitney U-test). **(vi)** Fixed and fresh fat tissue show that adipose nuclei are asymmetric and flattened proximal to FDs when compared to nuclei in non-fat cells (n = 38 cells, N = 2, *, P < 0.05, using Mann–Whitney U-test). The nuclear aspect ratio of fat cells also shows greater nuclear deformation than MSCs on stiff gels or rigid plastic (n = 250 cells, *, P < 0.05, significance between each of the conditions is determined by Mann–Whitney U-test). The error bars in the box plots are the 95% confidence interval, red lines indicate the median, and black lines are the means. **(B i)** FDs in U2OS cells after oleic acid addition (day 3) again show FDs in the approximately micrometer range (1.5 µm median diameter; n = 1,800, representative of N = 3 experiments). Inset: FD-containing cells show suppression of F-actin (n = 100, cells, N = 3 experiments, *, P < 0.05, determined by two-tailed t test). **(B ii)** Nuclear indentations caused by FDs (arrows) show higher deviation from a smooth, convex shape (n = 30 cells, *, P <0.05, two-tailed t test). **(B iii)** FDs maintain the same spherical shape whether indenting nuclei or not (yellow or gray arrow, respectively; n = 75 cells, *, P < 0.05, by Mann–Whitney U-test). **(B iv)** At sites of nuclear indentation (orange arrows), stiff F-actin fibers are indented by FDs (white arrows) and may also serve as a backstop promoting nuclear indentation. **(B v)** Treatment with F-actin disruptor Latrunculin-A for 90 min suppresses indentations and contact areas between FDs and the nucleus (n = 200 FDs in 30 cells, K–S test, *, P < 0.05, representative of duplicate experiments). All error bars are means ± SEM. **(C i and ii)** Confocal mid-sections of nuclear indentation by small FDs show consistent depletion of Lamin-B1, which frequently contrasts with Lamin-A,C (yellow arrowheads). Line plots quantify immunofluorescence intensities along the envelope, and bar graph quantifies Lamin-A,C's more varied response at indentations (n = 70, N = 3). **(C iii)** Relative densities of Lamin-B1 measured at sites of FD indentation (n = 65, N = 5 experiments). The results fit a rigid filament-binding model (R^2 = 0.72; see text and Materials and methods). Model parameters are (best fit: ε = 3.9, B = 0.51, α = 10.8) or (constrained fit: ε = 4.65, B = 0.50, α = 12.8). Lamin-B1 depletion is unaffected by knockdown of Lamin-A,C (open points; n = 15 cells, duplicate experiments). Inset: As a function of curvature, Lamin-B1 dilution fits the single filament model (R^2 = 0.72: ε = 3.9, B = 0.51, α = 10.7). **(C iv)** Sketch: Lamin-B1 filaments (red) with farnesylation groups (black lines) consistently detach and deplete from high Gaussian curvature sites, which could favor nuclear rupture despite the more varied response of Lamin-A,C. All error bars are means ± SEM.

particular, Gaussian curvature (typified by a bowl shape) has been speculated to be of greater importance than mean curvature (a wrinkle or fold; Fig. S1 B). Based on the above, we specifically hypothesize that small, micron-size FDs possess sufficiently high interfacial tension to act as spherical indenters and disrupt nuclear integrity, particularly for cells with low Lamin-A,C that seem more reliant on their constitutive Lamin-B. Key results here question a notion that Lamin-B does not regulate nuclear mechanics (Lammerding et al., 2006) and show curvature-dependent perturbations to lamin density, and nuclear rupture with mislocalization of DNA repair factors plus increased DNA damage.

Results and discussion

FDs displace and deform the nucleus and cytoskeleton, with small FDs seeming rigid

Adipogenesis of MSCs is extensive in adult human bone marrow and is seen in vitro to suppress actomyosin levels (Fig. 1, A iv), consistent with known remodeling of the actin cytoskeleton (Spiegelman and Farmer, 1982; Verstraeten et al., 2011). Whereas actomyosin stress is sufficient to drive nuclear deformation and even nuclear rupture when lamins are repressed (Hatch et al., 2013; Tamiello et al., 2013; Xia et al., 2018), nuclear indentations in MSCs seem to associate here directly with perinuclear FDs that vary in diameter from 3 to 7 µm (Fig. 1, A v). The giant FD in a mature tissue adipocyte also deforms the nucleus compared to nearby non-adipocytes that remain symmetric (Fig. 1, A iii and vi). All of the tissue nuclei are also highly elongated (Fig. 1, A vii), consistent with a high local rigidity based on comparison with nuclear elongation of MSCs on stiff versus soft substrates (Böddeker et al., 2022; Swift et al., 2013). These initial observations suggest an interplay of FDs with the nucleus and cytoskeleton in tissue-relevant cells, but further insight could benefit from an experimentally tractable model system.

Osteosarcoma cells derive from mesenchymal cells in bone (Pontén and Saksela, 1967), and the particular U2OS line studied here has been used to study adipogenic processes (Mohseny et al., 2011). Addition of oleic acid to cultures is common (Bersuker et al., 2018; Pfisterer et al., 2017) and relevant to FD formation in cancer cells (Nieman et al., 2011). Cytoplasmic FDs with a ∼1.5 µm median diameter are seen in a day (Brasaemle and Wolins, 2006; Mannik et al., 2014); they eventually fill a similar area of cytoplasm as the nucleus (Fig. 1, B i and Fig. S1 C) and modestly suppress F-actin levels (Fig. 1, B i inset). Nuclear indentation in U2OS cells is evident in about 30% of cells and tends to roughen the perimeter (Fig. 1, B ii).

Small FDs that indent a nucleus are always round and in the micron range (Fig. 1, B iii). Confocal z-stacks also show no flattening of FDs, with profiles similar to polystyrene micro-beads (Fig. S1 D). The thick stress fibers in U2OS cells (Hotulainen and Lappalainen, 2006) are bent by the FDs (Fig. 1, B iv and Fig. S1 E), with effective diameters (<2 µm) that are small compared to the ∼10 µm persistence length of even a single actin filament (Gittes et al., 1993). Rescue of the indentations with Latrunculin (90 min) increases the distance between FDs and the nucleus, suggesting that actomyosin helps push small FDs into nuclei (Fig. 1, B v), but roles for other factors (e.g., nesprins) require further study. Also, FDs smaller than ∼1 µm are likely to be too small to have the observed effects.

Confocal sections through FDs that indent the nucleus reveal that Lamin-B1 dilutes reproducibly, whereas Lamin-A,C varies, and the slightly elevated DNA intensity at the envelope (heterochromatin) shows little change (Fig. 1, C i and ii). Lamin-B1's density also decreases with indent diameter associated with Gaussian rather than mean curvature, and its dilution proves independent of Lamin-A knockdown (Fig.1, C ii and iii; and Fig. S1, F–H). The stoichiometric ratio of Lamin-A:B dictates nuclear stiffness and strength, and the ratio for MSCs is ∼5–10, whereas for cancer cells such as U2OS cells, the ratio is often low despite

the mechanosensitivity of Lamin-A,C (Irianto et al., 2016; Swift et al., 2013). GFP–Lamin-B receptor (LBR; Fig. S1 I), which binds Lamin-B1 (Olins et al., 2010), also shows FD-induced depletion, and we see the LBR-demarked ER is often distant from FD indentations, which is notable because of FD biogenesis in the ER (Thiam et al., 2013).

Lamin filaments have a persistence length in situ of ∼1 µm (Turgay et al., 2017), and such rigidity should disrupt the farnesylation-mediated attachments of Lamin-B1 filaments to a highly curved nuclear membrane (Fig. 1, C iv); hence, Lamin-B filaments can be expected to diffuse and bind to flatter regions of the nuclear membrane. Lamin-A,C lacks farnesylation and its response at the indentation site varies from accumulation to slight dilution compared to the reproducible local depletion of Lamin-B (Fig. 1, C ii and iii; and Fig. S1 G). Our sketch suggests a "single filament model" of curvature-driven membrane detachment (see Materials and methods) of the form:

$$\gamma = \frac{B}{1 + e^{\varepsilon - \alpha x}},$$

where γ is the amount of lamin dilution relative to a flat membrane, x is nuclear membrane curvature, B sets a minimum dilution, and ε (in k_BT units) and α are a membrane binding energy and curvature-dependent interaction factor, respectively. The equation is the same form as that used, for example, to fit the pressure-dependent activation of membrane Piezo channels (Coste et al., 2010) and fundamentally captures the molecular mechanism. Our measurements of Lamin-B1 depletion (Fig. 1, C iii) are fit well by such a sigmoidal equation even when ε is constrained to a value that fits outward Gaussian curvature (Pfeifer et al., 2022).

At sites of high outward nuclear curvature (i.e., nuclear poles), spontaneous nuclear rupture is evident after knockdown of Lamin-B1 or Lamin-A,C in standard 2D cultures of U2OS cells (Hatch et al., 2013; Xia et al., 2018). Given such protection conferred by both lamins to U2OS nuclei, we sought to address whether FD indentation and the reproducible local depletion of Lamin-B1 would sometimes cause nuclear rupture in wild-type U2OS.

Small fat droplets contacting the nucleus cause nuclear rupture, with loss of DNA repair factors

To look for rupture, U2OS cells were transfected with mCherry-cGAS (i.e., cyclic GMP-AMP synthase), which is a "DNA sensor" that diffuses in the cytoplasm but will enter an interphase nucleus at sites of nuclear rupture and persistently bind chromatin for many hours (Denais et al., 2016; Harding et al., 2017; Raab et al., 2016). Nuclear foci of cGAS at FD indentation sites coincide with Lamin-B1 depletion and slight DNA accumulation (Fig. 2, A i; and Fig. S2, A and B), and live imaging over 3 h clearly shows nuclear cGAS foci rapidly form at sites of FD-nucleus interaction (Fig. 2, A ii; and Fig. S2, C i and ii). Such foci are rare in cells when FDs are not near the nucleus; conversely, only a fraction of indents shows rupture.

Live-cell studies done at day 1 with sparse FDs are best to relate a specific FD with a rupture site. Foci intensity of cGAS saturated by ∼30 min, remained stable for >90 min, extended several µms from the site of FD–nucleus interaction, and showed local densification of chromatin (Fig. 2, A ii and iii; and Fig. S2, A and B). GFP–Lamin-A expressing cells suggest accumulation of Lamin-A at cGAS-marked rupture sites (Fig. S2 B), in agreement with laser-triggered rupture (Kono et al., 2022). Mobile cGAS not only enters a ruptured nucleus (Fig. S2, C i and ii) but might also undergo liquid-to-solid gelation beyond ∼1 h (Du and Chen, 2018). Pre-existing cGAS foci or "scars" in ∼20% of FD-laden cells indicate past rupture events that remain stable over ∼hours, consistent with sustained binding (∼6–9 h from comparing to live imaging); the cGAS scar frequency certainly exceeds the combined ∼10% observed during the 3 h of live-cell imaging and ∼5% seen as preexisting foci in cells with no FDs near the nucleus (Fig. 2, A iv; and Fig. S2, C iii and iv). Whereas GFP–Lamin-A overexpression suppressed cGAS foci in cells with FDs, multiple cGAS scars in a single nucleus are more common in Lamin-A,C knockdown cells (Fig. S2, B v). Importantly, all cGAS entry events in live imaging were associated with FDs < 3.5 µm, consistent with Lamin-B1 dilution (Fig. 1 C).

To further assess spatiotemporal dynamics of cGAS accumulation at a rupture site, we locally indented and ruptured nuclei in intact cells by using an Atomic Force Microscope (AFM) with a high curvature tip (<100-nm-diameter tip), a dwell time of 30 s, and forces of ∼10 nN (Fig. 2, B i). cGAS spreads again over several micrometers from the contact site (Fig. 2, B ii), which mimics focal rupture by FDs (Fig. 2, B iii vs. Fig. 2, A i and ii; and Fig. S2 A).

Nuclear exit of a diffusible DNA repair factor was our next focus in live-cell imaging of FD-induced rupture, and GFP-KU80 was chosen because it is predominantly nuclear but can transiently mislocalize to cytoplasm upon nuclear rupture (Fig. 2 C; Irianto et al., 2017; Xia et al., 2018). Small FDs within a few micrometers of the nucleus edge were tracked over time in cells with sparse FDs and showed modest changes in FD-to-nucleus distance over ∼10 min timescales, suggestive of oscillatory FD motility (Fig. 2, C i; Valm et al., 2017; Welte, 2009). FDs that transiently localized at the nuclear rim often associated with a sudden decrease in nuclear GFP-KU80 simultaneous with an increase in cytoplasmic GFP-KU80 (Fig. 2, C ii; and Fig. S2, D i and ii). Nuclear signal recovered after ∼1–2 h, which is longer than recovery of smaller GFP-NLS constructs in other rupture studies (Robijns et al., 2016; Xia et al., 2018). Although less than half of all FD-nuclear close-contacts showed nuclear rupture (Fig. 2, C i stars), overall ∼13% of cells loaded with FDs showed real-time mislocalization of GFP-KU80—exceeding rupture frequency of controls (Fig. 2 D) and consistent with fixed cell results and live tracking of rupture using cGAS (Fig. 2, A iv). Importantly, all KU80 mislocalization events associated with FDs <3.5 µm, consistent again with Lamin-B1 dilution (Fig. 1 C), whereas low curvature indentations were not sufficient to rupture nuclei and mislocalize KU80 (Fig. S2, C iii).

Fat droplets increase DNA damage and cell-cycle defects in 2D and after 3D migration

Based on loss of key DNA repair factors for hours, we next hypothesized that FD-loaded cells with nuclear rupture would exhibit more DNA damage. Immunostaining for the DNA

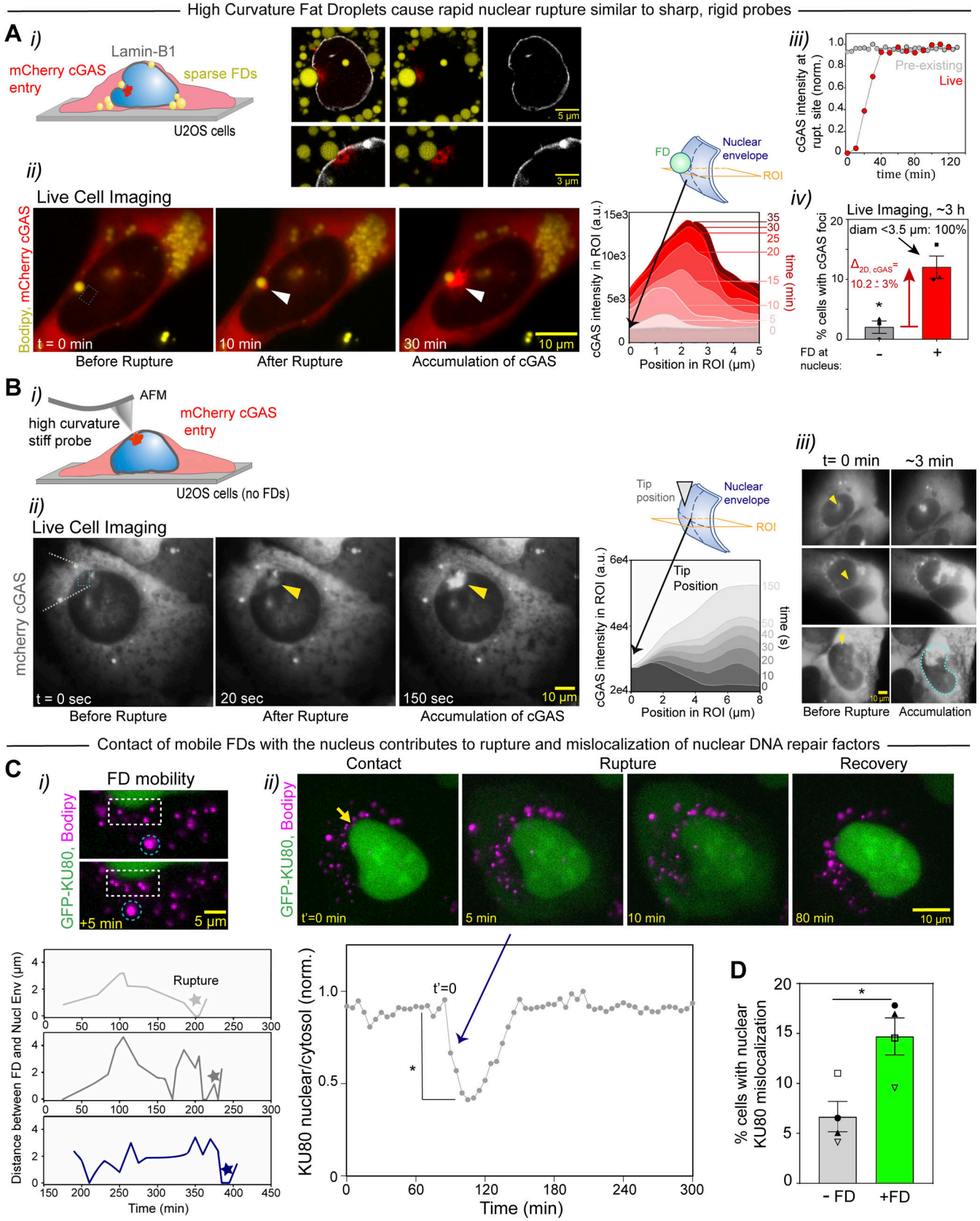

Figure 2. **High curvature FDs rupture the nucleus similar to stiff AFM probes, causing rapid accumulation of cGAS at rupture sites and mislocalization of DNA repair factor to cytoplasm. (A i)** Cytosolic DNA sensor cGAS accumulates and Lamin-B1 depletes at sites of interaction with high curvature FDs in fixed cells (representative of $N = 3$, $n = 10$ cells). **(A ii)** Live imaging of cGAS accumulation over 3 h at the nuclear edge after FD contact

(arrowhead). Intensity plot for the region of interest (ROI: yellow rectangle) shows cGAS accumulation by 10 min and saturation at 30 min. **(A iii)** cGAS intensity at rupture sites remains high for hours as a "cGAS scar." **(A iv)** Cells with FDs co-localized at the nucleus or not were scored for cGAS foci during live imaging, with more of the co-localized cells showing foci ($N = 3$, $n = 18$, *, $P < 0.05$, two-tailed t test). All error bars are means ± SEM. **(B i and ii)** A stiff AFM probe of high curvature is pressed into the nucleus. cGAS accumulates (arrowhead) on micrometer scales over minutes, indicating rupture. A constant intensity of cytoplasmic cGAS indicates the plasma membrane does not rupture. **(B iii)** Further examples of cGAS accumulation (arrowheads) within ∼3 min of initiating nuclear rupture ($N = 3$, $n = 20$). **(C i)** Live-cell imaging of FD mobility within cytoplasm allows measurement of a fluctuating distance to the nucleus. The minimum distance often coincides with mislocalization of DNA repair factor GFP-KU80 to cytoplasm, indicating nuclear rupture (star; $n = 4$, representative of duplicate experiments). **(C ii)** Mislocalization within minutes of contact of a moving FD (arrow) is followed by a slow recovery into the nucleus ($n = 30$, $N = 2$, *, $P < 0.05$, Mann–Whitney U-test is used to test the significance of the intensity drop at rupture). Cells were imaged for 7 h at day 1 after FD induction, when FDs remain sparse. All error bars are means ± SEM. **(D)** Mislocalization of KU80 to cytoplasm for FD-loaded and control U2OS cells is compared in live and fixed samples, with the FD-loaded cells having a higher frequency (open or closed symbols, respectively: $n = 370$ or 500 cells, $N = 4$, *, $P < 0.05$, two-tailed t test). All error bars are means ± SEM.

damage marker γH2AX have associated damage with nuclear rupture after Lamin-A knockdown in standard 2D culture (Xia et al., 2018). FD-laden cells with cGAS$^+$ nuclear rupture likewise show high DNA damage relative to a basal level regardless of FDs (Fig. 3 A). Therefore, FDs do not increase DNA damage through other mechanisms. Nuclear rupture in the absence of FDs tends to slightly elevate DNA damage, but the higher frequency of rupture with FDs (Fig. 2 D) can be anticipated to maximize damage. DNA damage can trigger checkpoint(s) that impede cell cycle as we have recently shown with Lamin-A suppression in beating hearts from chick embryos and in standard 2D cultures of cardiomyocytes (Cho et al., 2019). FD-loaded cells here indeed show an increased fraction of cells in S-phase (Fig. 3 B), suggesting that FDs can initiate indentation → damage → cell cycle perturbation (Fig. 3 C). Rescue of rupture-induced DNA damage and cell-cycle delay is indeed achieved in part by overexpressing KU80, KU70 plus one more repair factor (Xia et al., 2019).

To further assess the effective stiffness of the small FDs and their impact on other cell functions relevant to MSCs and some FD-containing cancers, such as migration (Cruz et al., 2020), we plated the U2OS cells with or without FDs at high density on Transwell membranes with highly constricting 3-μm-diameter pores and then fixed, stained, and imaged by confocal microscopy after 24 h (Fig. 3 D). The vast majority of FDs (>90%) are smaller than the chosen pore size (Fig. 1, B i), and we find many examples of FDs that co-localize with a nucleus within a pore (Fig. 3, D i). Importantly, the nucleus deforms but the FD remains round, even for ∼2 μm FDs that strongly distort the nucleus as the rigidity of the pore back-stops the nuclear indentation (instead of actomyosin stress fibers per Fig. 1, B iv). The results further underscore the rigidity of FDs.

Given that FDs suppress F-actin and indent actomyosin fibers (Fig. 1, B i and iv), we anticipated an impact on actomyosin function such as the rate at which a cell pulls itself through a constricting pore (∼3 h) to migrate from top to bottom of a Transwell (Xia et al., 2019). Indeed, fewer of the FD-loaded cells migrated in the same period as control cells (Fig. 3, D ii), with almost as much suppression as occurs with myosin-II inhibition of U2OS cells (Fig. S3, A i). Nuclear indentation by the rigid FDs in pores might also impede migration, but the small fraction of such cells (∼10% of nuclei in pores; Fig. 3, D i) would not account for the much larger effect on constricted migration.

Constricted migration through 3 μm pores is known to deplete Lamin-B and causes rupture at high curvature poles, but also dysregulates DNA repair factors and impedes cell cycle (Irianto et al., 2016; Irianto et al., 2017; Pfeifer et al., 2018; Xia et al., 2019). FDs increase all of these processes (Fig. 3, D iii and iv; and Fig. S3, A ii and iii), and ruptured nuclei again show maximum DNA damage (Fig. 3, D v) with FDs delaying cell cycle in the well-spread cells on bottom as in 2D culture (Fig. 3, D vi). Generally, FD-induced scars of lamin-B1 and nuclear cGAS are two- to threefold more frequent than the transient KU80 mislocalization (Fig. 2 D; and Fig. 3, D iii and iv; and Fig. S2 B). Mislocalization of KU80 is less clear on the Transwell top, likely because cell density is so high (in order to drive migration) that cells and nuclei remain rounded; this typically reflects limited actomyosin fiber assembly and would predict limited FD indentation (per Fig. 1, B iv). Nonetheless, Lamin-B1 dilution can be found at sites of FD indentation, whereas nuclear wrinkles—which have no Gaussian curvature—show no Lamin-B1 dilution (Fig. S3 B). The results overall provide further evidence for the indentation-damage-cell-cycle checkpoint pathway caused by FDs (Fig. 3 C) and again highlight an effective rigidity of FDs.

Interfacial tension is indeed high for FDs in tissue adipocytes

Our various in vitro observations of small FDs interacting with nuclei—starting with our original observations of nuclear indents (Swift et al., 2013)—all indicate that small FDs deform the nucleus rather than vice versa. To begin to quantify the mechanically key γ (Fig. 1, A ii), visceral fat tissue was freshly isolated from mice and aspirated into micropipettes with supracellular diameters (∼50–100 μm; Fig. 4, A i). This method has been used to measure the elasticity of embryonic heart and the viscoelasticity of brain (Cho et al., 2019). With a sufficient step in aspiration pressure, the tissue distends into the micropipette and slowly flows; a creep compliance power law exponent $\alpha < 0.2$ indicates a near solid-like response (Fig. 4, A ii and Fig. S3 C). Such isolated tissue has ECM including multicellular fibers (Fig. 4, A i) that likely modulate the mechanics (Heid et al., 2014) and that usually indicate a basal stress and a modest stiffness for fat tissue (∼1–3 kPa; Alkhouli et al., 2013). This agrees with our past findings that fat tissue has intermediate levels of fibrillar collagens as well as Lamin-A,C (Swift et al., 2013), which likely reflects the large FDs acting as mechanical stressors within the tissue. Indeed, inverting our creep compliance values at 1 s indeed gives similar values for cells and tissue (∼3–5 kPa) that is several-fold stiffer than brain, which is softer and has very little lamin-A,C and collagen. However, compared to a rigid

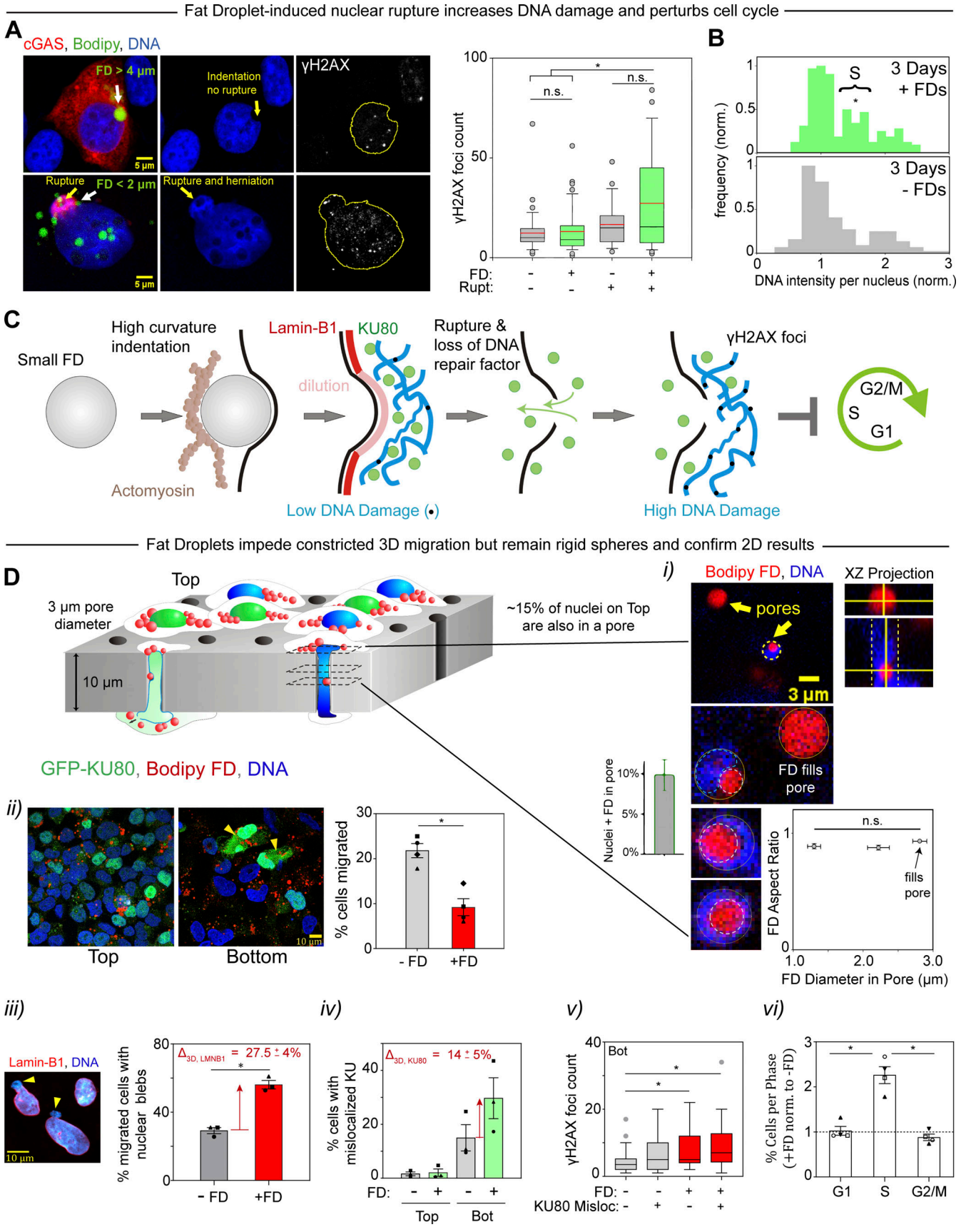

Figure 3. **DNA damage and cell-cycle perturbation are increased with FD-induced nuclear rupture, with similar FD-disruptive effects in 3D-constricted migration. (A)** FD-ruptured nuclei (cGAS$^+$) show more DNA damage when compared to non-ruptured controls. Top row images show a large

FD indents the nucleus (arrow) without rupture based on cGAS remaining cytoplasmic. Bottom row images show rupture (arrow). Immunofluorescence staining for γH2AX foci is done 1 d after FD induction (n = 135 cells, duplicates, *, P < 0.05, significance was determined by K–S test). Error bars are the 95% confidence interval, red lines indicate the median and black lines are the means. **(B)** Cell cycle of FD-loaded cultures is perturbed by FDs, with more cells in S-phase. Total DNA intensity per nucleus is normalized and used to determine cell-cycle stage (n = 350 cells, N = 3, *, P < 0.05, K–S test). **(C)** Proposed pathway: Small, stiff FDs create high Gaussian curvature at indentation sites, in part due to a cytoskeletal backstop, and indentation dilutes Lamin-B1, favoring nuclear rupture, rapid mislocalization of DNA repair factors, increased DNA damage, and perturbed cell cycle. **(D)** Cells plated on Transwell tops 1 d after FD induction were allowed to 3D-migrate through 3-µm-diameter pores for 24 h. **(D i)** Cross-section confocal slices from within Transwell pores show FDs remain round (arrows) even while they distort the pore-deformed nuclei (n = 13, N = 2). **(D ii–iv)** Fewer cells with FDs migrate to bottom vs. controls (n = 400 cells, N = 4, *, P < 0.05), and yet ∼twofold more FD-loaded cells show rupture with Lamin-B1–deficient nuclear blebs (arrowheads; n = 450 cells, N = 3, *, P < 0.05) and mislocalization of DNA repair factors (circle, square = KU80; triangle = KU70; n = 360 cells, N = 3, *, P < 0.05). **(D v and vi)** Migrated FD$^+$ cells with nuclear rupture maximize γH2AX foci (n = 120; K–S test, *, P < 0.05), and FD$^+$ cultures again show more cells in S-phase with a tendency for G2/M suppression (filled = 3D, open = 2D; n = 500 cells, N = 4, *, P < 0.05). For all bar graphs, significance was determined using two-tailed t test.

osteogenic phenotype, adipogenesis of MSCs is favored on soft matrix and by partial knockdown of lamin-A,C (Swift et al., 2013), and a nuclear stiffness of ∼2 kPa for cells on soft matrix decreases by half or more after knockdown (Ivanovska et al., 2017). Such a nuclear stiffness multiplied by the FD's radius of curvature (Fig. 1, A ii) suggests γ >> 2 mN/m for micron-size FDs to remain round in nuclear indentation.

To measure γ for FDs in fresh fat tissue—which is a measurement we were unable to find in the literature—we mechanically isolated FDs from tissue via cycles of back-and-forth aspiration (Fig. 4, B i). Individual FDs flow in aspiration as viscoelastic materials that nearly equilibrate in ∼10–100 s (Fig. 4, B ii), per FRAP recovery timescales (Fig. S1 A). Release shows reversibility (Fig. S3 C), consistent with γ driving elastic recovery to a minimum area sphere. Applying the Young-Laplace equation to distensions near equilibrium gives γ ∼40 ± 4 mN/m (Fig. 4, B ii plot). This is higher than that of FDs from cultured kidney cells and fly hemocyte-like cells but typical for oil–water interfaces (Israelachvili, 2011; Fig. 1, A ii). FDs from tissue could have distinct factors that affect γ, but FDs possess sufficient rigidity to remain spherical as they indent a nucleus.

Macrophages: Small FDs and phagocytosed beads indent and dilute Lamin-B1

Macrophages accumulate FDs in atherosclerosis and obesity among other conditions (Castoldi et al., 2020; Yang et al., 2022), and human THP-1 macrophages provide a physiologically relevant model in wide use (Chanput et al., 2014; Mejhert et al., 2020). Endogenous FDs are micron-size and remain round as they displace the actomyosin (Fig. 5 A), but compared to U2OS cells, the nucleus seems less tensed (as less ellipsoidal) and the cells are less spread. Peri-nuclear actomyosin fibers are indeed rare, and Lamin-A:B stoichiometry is high versus U2OS cells (Fig. 5 B), but micron-size FDs induced by oleic acid (Fig. 5 C and Fig. S1 C) again indent the nucleus and dilute Lamin-B1 (Fig. 5 D).

Large FDs are deformed in tissue (Fig. 1, A iii) and also in some cell-culture models (Loneker et al., 2023), which raises questions about their ability to act simply as mechanical stressors. Large FDs also associate with lipases (Schott et al., 2019) and nuclear lipases couple to membrane integrity and tension (Lomakin et al., 2020; Venturini et al., 2020). To therefore assess a biophysical basis for indentation dilution, the macrophage cytoplasm was loaded with 3-µm rigid beads by phagocytosis (Fig. 5, E i and ii). Gaussian curvature at sites of bead indentation (Fig. 5, E ii, lower image) shows local depletion of Lamin-B1 (Fig. 5, E iii) that is slightly lower than that for larger FDs in macrophages (Fig. 5 F) but consistent with U2OS trends (Fig. 1, C iii). Nuclear rupture is less likely because of higher Lamin-A,C as well as low tension on the THP-1 nucleus, but the results support our overall hypothesis that FDs possess sufficient rigidity to mechanically stress the nucleus.

In conclusion, Gaussian curvature–dependent dilution of Lamin-B is a consistent observation across inward (Figs. 1, 2, 3, and 5) and outward curvature scenarios (Pfeifer et al., 2022; Xia et al., 2018). In comparison, Lamin-A,C varies with a rate- or rupture-dependent response (Kono et al., 2022; Pfeifer et al., 2022), but mechanoprotects against rupture and likely explains why Lamin-A,C expression levels in tissues scale with the operating stress and stiffness of a mature or developing tissue (Cho et al., 2019; Swift et al., 2013). Consistent with such a mechanism and the phase-separated nature of FDs as oil in water, adipogenic differentiation shows decreases in Lamin-A,C levels (Verstraeten et al., 2011) accompany the progressive increases in FD size—which corresponds reasonably well to decreased curvature stress (Fig. 1, A ii).

Materials and methods

Cell culture

U2OS cells (gift from Roger Greenberg, University of Pennsylvania) with genotype confirmed the Discher lab (Irianto et al., 2017) were cultured in DMEM high glucose medium (Gibco) supplemented with 10% FBS (Sigma-Aldrich) and 1% penicillin/streptomycin (Gibco). Bone marrow–derived MSCs were isolated from bone marrow aspirates obtained from posterior iliac crest of anonymous human donors (University of Pennsylvania Stem Cell Core, with Institutional Review Board approval) under the procedures and regulations defined by the Helsinki agreement. Mono-nucleated cells were depleted from CD34-positive cells by a microbead kit (Direct CD34 Progenitor Cell Isolation Kit, Miltenyi Biotec) and screened by automated cell separation (AutoMacs, Miltenyi Biotec) according to manufacturer's protocols. Cells were cultured in standard tissue culture flasks in low-glucose basal medium (DMEM, Life Technologies), supplemented with 10% FBS (Sigma-Aldrich) and 1% penicillin/streptomycin antibiotics (GE Healthcare) and incubated at 37°C and 5% CO_2 humidified conditions. After 24 h cells were thoroughly rinsed (3× times) with PBS to remove non-adherent cells. After

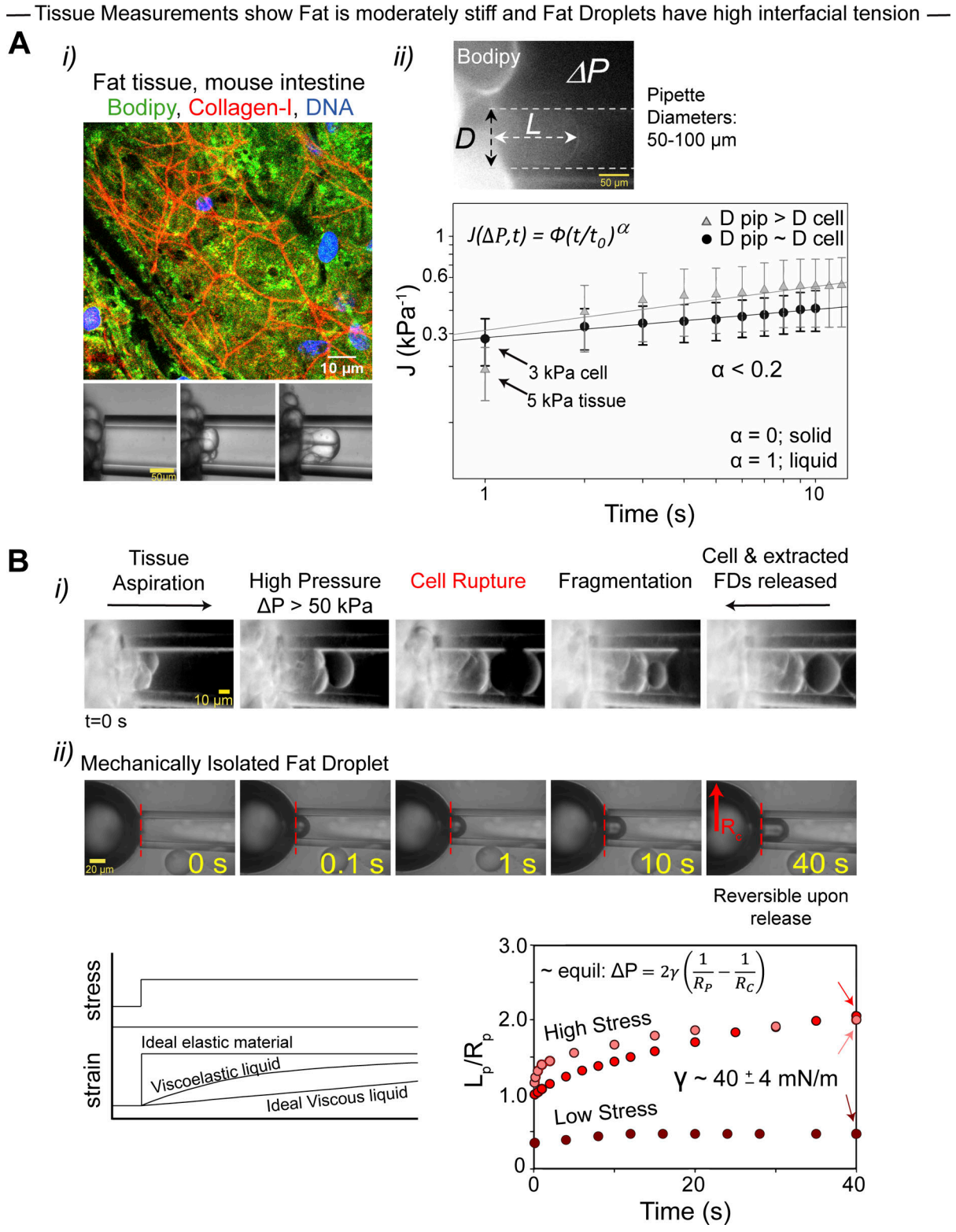

Figure 4. **Fat tissue is solid-like and moderately stiff based on micropipette aspiration, with mechanically isolated FDs exhibiting a high interfacial tension similar to oil–water. (A i)** Fat tissue stained with lipophilic Bodipy dye possesses a collagenous network visible by immunofluorescence in confocal images. Micropipette aspiration reveals individual fat cells. **(A ii)** Under aspiration pressure ($\Delta P \sim 5$ kPa), the compliance of fat tissue exhibits a weak power law, which is a signature of a predominantly solid-like, viscoelastic response ($n = 8$ tissues from four mice). **(B)** FDs were mechanically extracted from fresh fat tissue to measure an effective interfacial tension of FDs. **(B i)** Tissue was aspirated at high pressure ($\Delta P = 50$ kPa) causing membrane rupture and cell fragmentation before release. **(B ii)** Released FDs were re-aspirated. Sketch: A purely elastic material should respond instantly, and a viscous material should respond slowly. Plot: Application of the Young-Laplace equation to a near equilibrium strain gives an interfacial tension of ~40 ± 4 mN/m ($n = 3$).

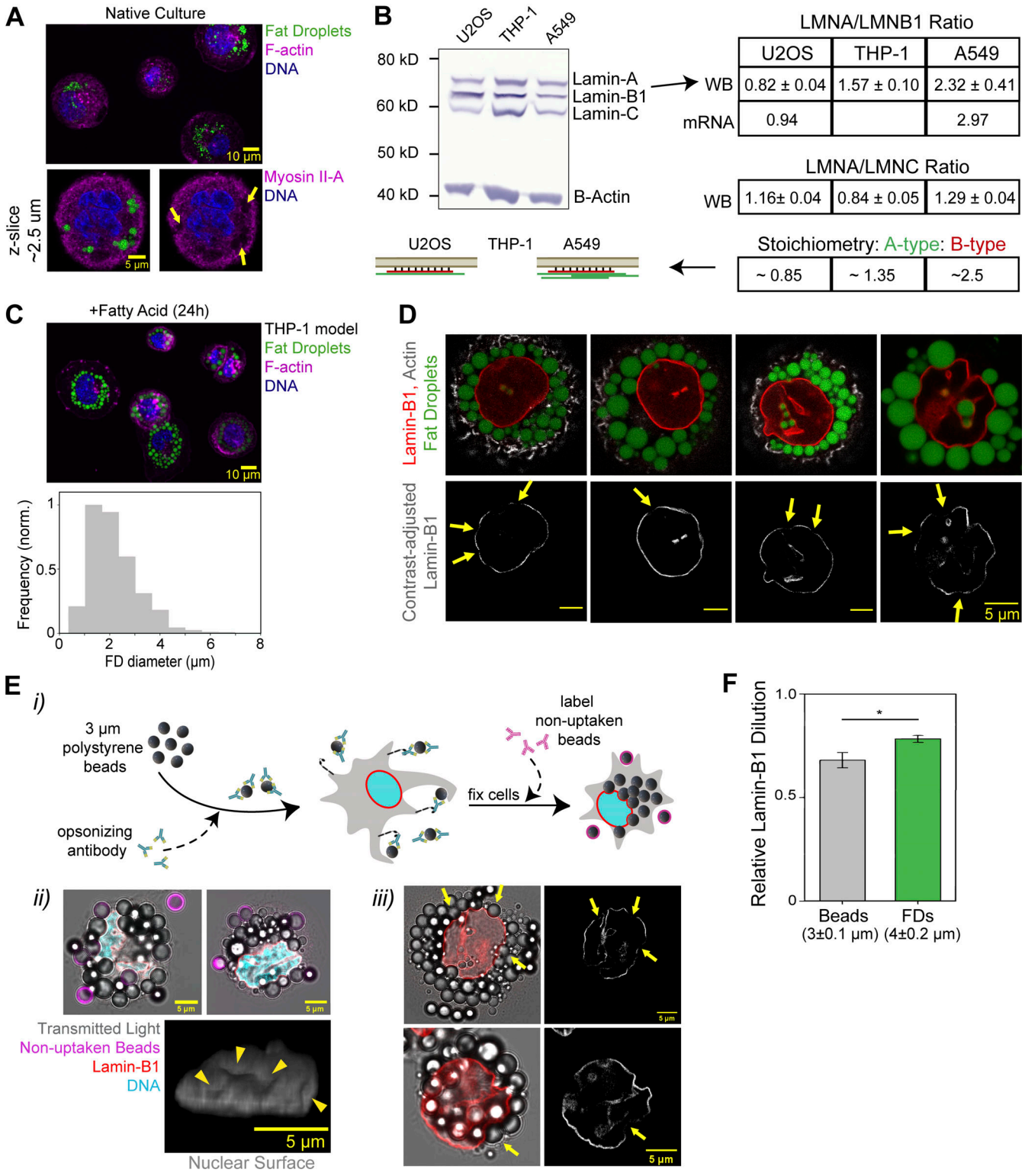

Figure 5. **Macrophages also show indentation dilution of Lamin-B1 by FDs and by beads. (A)** THP-1 macrophages show endogenous, small FDs (Bodipy dye), and z-slices from confocal imaging show FDs exclude myosin-IIA (arrows). **(B)** Immunoblot of lamins shows the ratio of Lamin-A to -B1 is low in U2OS osteosarcoma cells relative to THP-1 macrophages and A549 lung adenocarcinoma (normalized to B-actin). For all cell types, the immunoblot also shows Lamin-C ~ Lamin-A. Table: Mean ± SEM from immunoblots (n = 4, *, P < 0.05 for U2OS cell A:B1 ratios compared to others, two-tailed t test). Mean ratios of mRNA are calculated from cell-line expression data in The Human Protein Atlas database, and show the same trend. WB, Western blot. **(C)** Addition of oleic acid to macrophage cultures for 1 d showed most macrophages are FD filled. The histogram of FD diameters (n = 1,500 FDs, duplicates) indicates slightly larger FDs than in U2OS cells (compare to Fig. 1, B i). **(D)** Top: Four representative images of macrophages filled with FDs. All show focal indentation-dilution of

Lamin-B1. Black-and-white lower panel: Lamin-B1 signal is contrast-adjusted to visualize its depletion (arrows) relative to nearby nuclear lamina signal. **(E i)** Schematic of bead-loading into macrophages by Fc-Receptor mediated phagocytosis. This is done in order to assess any nuclear indentations. **(E ii)** Brightfield images with fluorescent overlays show bead-loaded macrophages and a few beads that are not internalized (magenta). Representative image of the nuclear surface in a bead-loaded macrophage shows distinct sites of bead-induced indentation (arrowheads). **(E iii)** Brightfield and anti–Lamin-B1 IF overlay shows lamina indentation caused by beads (arrows). Black-and-white right panel: Lamin-B1 signal is contrast-adjusted to visualize its depletion (arrows) relative to nearby nuclear lamina signal. **(F)** Lamin-B1 dilution at nuclear indentation sites in macrophages is caused by beads (~3 µm diameter) or else by FDs (4 µm diameter; errors are mean ± SEM, beads n = 16 and FDs n = 30, N = 3, *, $P < 0.05$, significance was obtained using Mann–Whitney U-test). A small difference is consistent with the curvature trend and model fit in Fig. 1, C iii.

3–4 d, colony-forming stromal cells appeared in the flasks, which were further expanded by passaging at ~80 confluency and re-seeding at ~50% confluency. Typically, cells from three different donors were mixed and used for the experiments. Flow cytometry was used to verify that cells are negative for hematopoietic markers (CD45-RA, CD34) and positive for stromal stem cells markers (CD105, CD166, CD44, and CD90). For adipogenic differentiation, bone marrow–derived MSCs were plated (5,000 cells per mm^2) on 6-well plates and induced with standard adipogenic media for 2 wk (R&D), following manufacturer protocol. THP-1 cells (ATCC, # TIB202) were cultured in RPMI 1640 medium (Gibco) and supplemented with 10% FBS and 1% penicillin/streptomycin. All cells were kept incubated at 37°C with 5% CO_2. To obtain macrophages, THP-1 monocytes were differentiated using PMA (Sigma-Aldrich) for 48 h in RPMI media. When drug treatment was necessary, U2OS cells were PBS-washed and media was replaced with complete media containing 1 µM Latrunculin-A (Sigma-Aldrich) and incubated at 37°C, 5% CO_2 for the specified time.

Fat droplet formation and fluorescence staining

Tris HCL–Hydroxymethyl Aminomethane Hydrochloride–and Tris Base (both from Thermo Fisher Scientific) were dissolved in deionized water and combined with Fatty Acid-Free BSA (Sigma-Aldrich). The resulting solution was supplemented with oleic acid (Sigma-Aldrich), well-mixed, and purified using a 0.20-µm syringe filter (Thermo Fisher Scientific). The resulting stock solution was mixed with complete DMEM media to obtain a final concentration of 1 mM (U2OS experiments) or complete RPMI media to a concentration of 400 µM (THP-1 experiments). Bodipy dye (Invitrogen, FL-C12 D3822 and 558/568, D3835) was added at a 1:1,000 dilution to the media–oleic acid mix prior to media replacement into pre-seeded well plates. Cells were incubated in the mixture for a duration of 24–72 h.

Immunostaining

Cell samples were fixed using 4% formaldehyde (Sigma-Aldrich) for 15 min, permeabilized using 0.5% Triton-X 100 (Sigma-Aldrich) for 10 min, and blocked with 5% BSA for 30 min at room temperature. Intermediate wash steps were conducted using 0.1% BSA in PBS. Cells were incubated in primary antibody at 4°C overnight. Antibodies utilized include: Lamin-A/C (1:500, mouse, 4C11; Cell Signaling), Lamin-B1 (1:500, rabbit, 16048; Abcam), myosin-IIa (1:50, rabbit, 34035; Cell Signaling), γH2AX (1:500, rabbit, 11174; Abcam), KU70 (1:500, mouse, sc-17789; Santa Cruz), and β Actin (1:300, mouse, cs-47778; Santa Cruz). Secondary antibody incubation (1:500, donkey anti-mouse 488, #A21202, 546, #A100036, 647, #A31571 or rabbit 488, #A21206, 546, #A10040, 647, #A31573; Thermo Fisher Scientific) occurred over 90 min at room temperature. Actin was visualized using Alexa Flour 647 phalloidin (A-31573; Invitrogen). Nuclei of cells were stained using Hoechst 33342 (H3570; Thermo Fisher Scientific) for 15 min.

Microscopy and live imaging

Lower magnification epifluorescence and brightfield images were obtained from an Olympus IX71 microscope with a 40×/0.6-NA objective and a digital EMCCD camera (Cascade 512B; Photometrics). Confocal image stacks were captured using either a Leica TCS SP8 system or a Zeiss LSM 980 system with a 63×/1.4-NA oil immersion objective. When mounting was necessary, fixed samples were placed between two glass coverslips wet with 15 µl antifade mountant (Prolong Gold and Prolong Diamond, Thermo Fisher Scientific) and allowed to set overnight. Experiments involving fixed, wet samples were performed, stained, immersed in PBS, and imaged within 35-mm coverglass-bottom dishes (MatTek) or chambered coverglasses (Thermo Fisher Scientific).

Live imaging experiments were performed at 37°C with 5% CO_2 using a Zeiss Axio Observer 7 with a 40× objective or an EVOS FL Auto 2 Imaging System with a 40× objective over the course of 3–7 h. Plates were imaged every 5–10 min to minimize photobleaching and cell death.

All images were processed with Fiji software (National Institute of Health) and fluorescent intensities, area measurements, and shape parameters were analyzed using the appropriate Fiji tools.

FRAP experiments

Freshly isolated mouse intestinal tissue was labeled with Bodipy for 2 h at 37°C. Confocal images were captured using a 20×/0.75-NA objective at different temperatures ranging from 24° and 37°C using a temperature-controlled stage on the microscope. In each experiment, a square area 25 × 25 µm was bleached using high laser power. Bleaching was minimized to >65% prebleach intensity in order to minimize any photoinduced damage or other adverse effects. Each recorded curve is then normalized to the prebleached intensity and corrected by subtracting the background intensity of the non-bleached section of the cell. The data were fitted with single exponent $I = I_0 + A(1 - e^{-\tau/t})$, where τ is the halftime of recovery of photobleaching.

Single-filament model

This parsimonious model (Pfeifer et al., 2022; Xia et al., 2019) considers a single stiff Lamin-B1 filament with an in situ length L_{fil} and persistence length l_p (Turgay et al., 2017). The filament is either attached to or detached from the nuclear membrane, giving a two-state partition function for the filament:

$$Z = \sum_s e^{-E_s/k_BT} = e^{-E_{attached}/k_BT} + e^{-E_{detached}/k_BT}. \quad (1)$$

The detached state is the reference state with $E_{detached} = 0$. For a flat nuclear membrane, $E_{attached}$ equals the negative binding energy, $-E$, which favors filament attachment. However, since the nuclear membrane can be curved (with curvature = $1/R$), two competing contributions to the energy of the attached state are considered:

$$E_{attached} = E_{binding} + E_{bending}. \quad (2)$$

$E_{bending}$, written as $\frac{1}{2}\frac{k}{R^2}$ (where k is the filament bending modulus), accounts for the energy cost of bending the stiff filament along the curved membrane, whereas $E_{binding}$ comprises the negative binding energy which favors filament attachment. $E_{binding}$ is modulated by membrane curvature because curvature can alter the filament-membrane contact area. Thus, Eq. 2 can be expanded to be written as a function of curvature:

$$E_{attached} = -E + \frac{a}{R} + \frac{1}{2}\frac{k}{R^2}. \quad (3)$$

The a/R term, where a is constant, captures the change in contact area between the nuclear membrane and Lamin-B1 filament resulting from induced curvature. The latter terms increase for decreasing R (i.e., higher membrane curvature), which means filament attachment becomes energetically costly at high membrane curvatures—and detachment more likely. The probability of the detached state is:

$$P_{detached} = \frac{1}{Z}e^{-E_{detached}/k_BT} = \frac{1}{1 + e^{\left(E - \frac{a}{R} - \frac{1}{2}k/R^2\right)/k_BT}}. \quad (4)$$

In the high-curvature limit, $1/R$ becomes very large and $P_{detached} \rightarrow 1$, consistent with a high probability of Lamin-B1 dilution and perhaps nuclear rupture at sites of FD-induced high membrane curvature (Fig. 1 D and Fig. 2, A and C). In the low curvature limit, $1/R \rightarrow 0$, $P_{detached} \rightarrow 1/(1 + e^{E/k_BT}) \rightarrow 0$, assuming $E >> k_BT$. A Lamin-B1 filament is thus unlikely to detach or dilute when low curvature is introduced by a large FD.

In this model, the term k depends on filament length L_{fil} and persistence length l_p: $k = (l_p k_B T)L_{fil}$. The values $L_{fil} = 0.38$ µm and $l_p = 0.5$ µm from Turgay et al. (2017) were utilized to calculate $k = (l_p\, k_B T)L_{fil} = (0.5\ \mu m;\ 0.38\ \mu m)k_BT = (0.19\ \mu m^2)k_BT$. Additionally, the bending term $\frac{1}{2}\frac{k}{R^2}$ has almost no effect on the best-fit curve when fitting data, so we exclude it. The form of the equation that fits the inset to (Fig. 1, C iii) per the main text:

$$y = \frac{B}{1 + e^{\varepsilon - \alpha x}}, \quad (5)$$

where B is a fit parameter, x is curvature, and ε and α are a relative binding energy and interaction energy, respectively. Here, FDs that interact with the nuclear membrane impose a curvature D, where D is most commonly the diameter of the FD indenting the nucleus. Thus, the equation may be rewritten as:

$$y = \frac{B}{1 + e^{\varepsilon - \alpha\left(\frac{2}{D}\right)}}, \quad (6)$$

where curvature is defined as 1/radius. Thus, the size of FD indentation is correlated with Lamin-B1 dilution. The measured dilution that fits the main plot of (Fig. 1, C iii) takes the form:

$$y = 1 - \frac{B}{1 + e^{\varepsilon - \alpha\left(\frac{2}{D}\right)}}. \quad (7)$$

Fit parameters have very similar values to those applied to nuclear rupture (Pfeifer et al., 2022; Xia et al., 2018).

Transfections or transduction

U2OS cells were transfected with mCherry-cGAS (from R. Greenberg, University of Pennsylvania; Harding et al., 2017), GFP-KU80 (from S.L. Rulten, University of Sussex, Brighton, UK; Grundy et al., 2013), or GFP-LBR (from R.-H. Chen, Academia Sinica, Taipei, Taiwan; Tseng and Chen, 2011) using a standard protocol (Xia et al., 2018). Briefly, Optimem (Gibco) was separately combined with Lipofectamine 2000 (Invitrogen) or the respective plasmid following the manufacturer's protocol. The two solutions are then mixed well and after 10 min, the mixture was added to antibiotic-free media before replacing the media in wells plated at 50–80% cell confluency.

Experiments to decrease Lamin-A gene expression were conducted as above using ON-TARGETplus Human Lamin-A (4000) siRNA—SMARTpool, 5 nmol, L-004978-00-0005 (Dharmacon) for transfection.

Lipid droplets were formed in the cells 24 h after transfection per Brasaemle and Wolins (2006) as described above.

The GFP–Lamin-A plasmid with EF1-α promoter (Izumi et al., 2000) was packed into a lentiviral delivery system for transduction of stably expressing U2OS cells. GFP–Lamin-A S22A plasmid was constructed by standard site directed mutagenesis (Stratagene). GFP-positive cells were sorted by flow cytometry and expanded.

Immunoblotting

For each sample, 1–2 million cells were trypsinized, pelleted, and resuspended in 1×radioimmunoprecipitation assay buffer supplemented with 1% protease and 1% phosphatase inhibitors before being sonicated for 15 s at intermediate power. After centrifugation at 4°C, samples were denatured at 90°C before addition of 0.5% β-mercaptoethanol and lithium dodecyl sulfate. Samples were loaded into a bis-Tris 4–12% gradient gel at 2 × 5, 10, and 15 µl for each sample and electrophoresis was performed (100 V × 10 min, 160 V × 55 min). Proteins were transferred onto a blotting polyvinylidene fluoride membrane using an iBlot Gel Transfer stack, Nitrocellulose, Mini (Invitrogen, Thermo Fisher Scientific) for antibody staining. Quantification of the blot to obtain the intensity ratios in the different cell lines was done by measuring the integrated intensity of the band of interest in Fiji, subtracting the background from a region of interest next to the band and calculating the ratio between the bands of interest.

Macrophage bead phagocytosis

Streptavidin-coated polystyrene beads (#SVP-30-5; Spherotech) were opsonized using anti-streptavidin primary antibody (1:500, #410501; Biolegend), centrifuged and washed, and added to complete RPMI media. The bead–media mix was incubated with differentiated macrophages for 3 h prior to fixation. Secondary antibody was added after fixation but before permeabilization of the cells to distinguish uptaken

and non-uptaken beads. Following bead labeling, immunostaining proceeded as above.

DNA damage and cell-cycle measurements

Cells were fixed and immunostained with γH2AX (see above). Foci were assessed and quantified in ImageJ using maximum signal intensity projections taken from raw confocal images stacks. 10 cells per field of view were randomly selected for manual counting of foci prior to application of a counting macro. The parameters of the counting macro that best reflected manual foci counts were applied to all other cell contours within the image. We measured DNA intensity for each nucleus based on Hoechst dye staining, and the main mode was used to normalize the histogram; this showed the maximum intensity was about twofold higher, as expected for genome duplication.

Transwell migration

Constricted migration assays were performed using 24-well inserts with 3-µm-diameter pores in polycarbonate membranes (Costar #3415; Corning). 1.5×10^5 cells were seeded on the tops of the membranes in complete media. FD-loaded cells were plated on tops of Transwells 24 h after addition of oleic acid. Complete media was also added to the bottom of the insert such that there was no nutrient gradient. The assay was kept incubated at 37°C and 5% CO_2 and allowed to proceed for 24 h. After 24 h, cells were fixed and membranes were detached from the insert for immunostaining as described above.

AFM indention during fluorescent imaging

Experiments were performed per Xia et al. (2018). Briefly, U2OS cells transfected with mCherry cGAS were replated on coverslips at a density of 60,000 cells/cm^2 and cultured overnight. Coverslips were mounted in the fluid cell of a hybrid AFM system (MFP-3D-BIO; software: MFP-3D + Igor Pro 6.05; Asylum Research; Oxford Instruments) equipped with an inverted optical fluorescence microscope (Olympus IX81 with 40×/0.60 NA objective). Experiments were performed in a closed liquid cell at a temperature of ∼29°C in DMEM high-glucose medium with 10% serum buffered at pH 7.4 with 25 mM Hepes to prevent cell death in the absence of CO_2. Cells were indented using MSCT-AUHW (Bruker) cantilevers with nominal spring constant 0.03 N/m, nominal tip radius 10–40 nm, and nominal tip height 2.5–8 µm. The cantilever spring constant was calibrated using thermal fluctuation method. The cantilever was positioned on the top of the nucleus, and the nucleus was indented with forces of ∼10 nN, which tended to rupture nuclei in roughly 50% of contacts. When the cantilever deflection reached a predefined set point, the tip would dwell on the spot for 100 s before the cantilever was retracted and detached from the cell. Simultaneous fluorescent images were captured every 10 s for the entire probing cycle, including before the force was applied and after the cantilever was retracted for several minutes. Ultimately, experimental results (Fig. 2 B) are single-cell experiments with images shown from different experiments. To maximize cell viability on the stage, experiments were carried out within ∼30 min, and after a cell was poked the dish and cantilever were tossed out to avoid tip contamination artifacts.

Image analysis of curvature and relative density of Lamin-B1 and Lamin-A/C

Quantification of indentation curvature and Lamin-B1 and Lamin-A/C relative density at curvature sites was examined using confocal slices captured every 400 nm. For analysis of the intensity of the lamina, cells containing an FD indenting the side of the nucleus causing an inward Gaussian curvature were used. Intensity profiles were obtained using line segments (length1 µm, thickness 2–3 pixels) drawn along the rim of the nucleus in xy plane over the z-slice that corresponded to the maximum indentation projection. Individual line segment profiles were combined to create intensity versus distance plots, which provided insights into the relative intensity change along the rim and within the indentation curvature (Fig. S1 F). The relative density of the lamins was obtained by taking the ratio of the mean intensity along the line at the indentation curve and along the lines adjacent to the curvature for comparable lengths. Intensity was measured in the corresponding imaging channels using the same profile lines.

Micropipette aspiration of fat tissue and mechanically isolated fat droplets

Fat tissue was excised from mouse intestine and immediately pulled using a homemade micropipette aspiration setup. Micropipettes were pulled from glass capillaries (World Precision Instruments) with 1-mm inner diameters using a Flaming-Brown Micropipette Puller (Sutter Instrument). Pulled tips were cut with ceramic tile to final inner diameter 50–100 µm. Pipettes were filled and treated for 20 min with 3% BSA in PBS to prevent sticking to the inside of the pipette. Pipettes were attached to a water-filled manometer-double reservoir of adjustable height. Pressures were applied with a combination of syringe suction and were measured using a pressure transducer (Validyne). Imaging was done on a Nikon TE300 epifluorescence microscope with a 40×/0.60 NA air objective and a digital EMCCD camera (Cascade, Photometrics). Fat tissue was placed in a glass chamber filled with CO_2 independent media and was aspirated at room temperature with pressures in the range of 1–50 kPa. The effective Young's modulus of the aspirated spheroids was obtained from the linear relationship between the pressure and the strain L/Rp for $L \leq Rp$,

$$\Delta P = \frac{2\pi}{3\varphi_0} E \frac{L}{R_p},$$

where ΔP is the pressure difference inside the pipette relative to outside, L is the length of tissue aspirated measured from the mouth of the pipette, Rp is the pipette's inner radius, and φ_o is a shape factor ∼2.

When a cell was aspirated at high pressure >50 kPa, cells rupture and the lipid are extracted and released into sample holder. The fat droplet that is formed in that way is aspirated again and the interfacial tension was calculated using Laplace's law.

Statistics

We adhered to the reproducibility requirements of the *Journal of Cell Biology*. Analysis and model fitting was conducted using

Prism (Graphpad) and SigmaPlot (SPSS). Unless otherwise indicated, plots display mean ± SEM, and *n* indicates the number of technical replicates (e.g., cells), with *N* indicating the number of biological replicates beyond duplicates. Statistical analyses were conducted using two-tailed Student's *t* tests when data passed normality tests (using Shapiro–Wilk test in SigmaPlot) and Mann–Whitney U-test was performed if the data did not pass a normality test. Data for fluorescent intensity were normalized by maximum raw intensity value. When data from multiple experiments were normalized to the control, one-sample *t* tests were conducted to test for statistical significance. K–S tests were used to compare distributions (FD distance to nucleus, DNA damage foci, and cell cycle). Significance is indicated with a star where appropriate in a figure or legend if $P < 0.05$.

Online supplemental material

Fig. S1 A contains data from FRAP experiments of freshly isolated mouse fat tissue at different temperatures. Fig. S1 B illustrates Gaussian curvatures with different signs. Fig. S1 C shows kinetics of FD area/nuclear area for U2OS and THP-1 macrophages. Fig. S1 D contains confocal images and data of the sphericity of indenting and not indenting FD calibrated with fluorescently labeled beads. Fig. S1 E contains images of actomyosin meshwork disruption by FDs and additional images of FDs induced displacement of actin fibers. Fig. S1 F illustrates the procedure used to quantify lamin intensity at sites of indentations. Fig. S1 G contains more images of Lamin-B1 and Lamin-A,C at different curvatures. Fig. S1 H shows Lamin-A,C expression levels in siLamin-A–treated U2OS. Fig. S1 I shows images and data about LBR depletion at FDs induced nuclear indentations. Fig. S2 A contains additional examples of colocalization of Lamin-B1 depletion and mCherry-cGAS accumulation at FD-induced rupture sites. Fig. S2 B shows images of GFP-LaminA–transduced U2OS. Fig. S2 C contains additional live-cell images of cGAS accumulation at rupture; multisite rupture, cGAS foci spatiotemporal kinetic; spatial correlation between cGAS foci and FD; rupture frequency in Lamin-A knockdown and overexpression; immunoblot of Lamin-A,C overexpression. Fig. S2 D contains additional live-cell images and kinetics of GFP-KU80 mislocalization due to FD-induced rupture. Fig. S3 A shows data of Transwell cell migration and compares the effect of FDs and blebbistatin on the migration efficiency and rupture frequency. Fig. S3 B shows FD-induced curvature with Lamin-B1 dilution and lamina wrinkle without. Fig. S3 C shows that isolated FDs have an elastic recovery.

Data availability

Data supporting the findings of this article are available in the published article and openly available in Figshare at https://doi.org/10.6084/m9.figshare.22722424.v1.

Acknowledgments

We thank Penn Microscopy Core's Dr. Andrea Stout and Jasmine Zhao for expert help.

Grants: Penn Center for Genome Integrity Pilot Grant; National Science Foundation DGE-1845298 (M.P. Tobin); Human Frontier Science Program RGP00247; National Institutes of Health U01CA254886; National Science Foundation DMR1720530; National Science Foundation CMMI1548571,154857; Pennsylvania Department of Health HRFF-4100083101.

Author contributions: I.L. Ivanovska, M.P. Tobin, and D.E. Discher designed experiments. I.L. Ivanovska, M.P. Tobin, and T. Bai performed the experiments. I.L. Ivanovska, M.P. Tobin, and D.E. Discher analyzed the data. L.J. Dooling provided mouse tissue for the experiments. I.L. Ivanovska, M.P. Tobin, and D.E. Discher wrote the manuscript.

Disclosures: The authors declare no competing interests exist.

Submitted: 25 August 2022
Revised: 24 March 2023
Accepted: 4 May 2023

References

Alkhouli, N., J. Mansfield, E. Green, J. Bell, B. Knight, N. Liversedge, J.C. Tham, R. Welbourn, A.C. Shore, K. Kos, and C.P. Winlove. 2013. The mechanical properties of human adipose tissues and their relationships to the structure and composition of the extracellular matrix. *Am. J. Physiol. Endocrinol. Metab.* 305:E1427–E1435. https://doi.org/10.1152/ajpendo.00111.2013

Anuurad, E., A. Bremer, and L. Berglund. 2010. HIV protease inhibitors and obesity. *Curr. Opin. Endocrinol. Diabetes Obes.* 17:478–485. https://doi.org/10.1097/MED.0b013e32833dde87

Ben M'barek, K., D. Ajjaji, A. Chorlay, S. Vanni, L. Forêt, and A.R. Thiam. 2017. ER Membrane Phospholipids and Surface Tension Control Cellular Lipid Droplet Formation. *Dev. Cell.* 41:591–604.e7. https://doi.org/10.1016/j.devcel.2017.05.012

Bersuker, K., C.W.H. Peterson, M. To, S.J. Sahl, V. Savikhin, E.A. Grossman, D.K. Nomura, and J.A. Olzmann. 2018. A proximity labeling strategy provides insights into the composition and dynamics of lipid droplet proteomes. *Dev. Cell.* 44:97–112.e7. https://doi.org/10.1016/j.devcel.2017.11.020

Bidault, G., C. Vatier, J. Capeau, C. Vigouroux, and V. Béréziat. 2011. LMNA-Linked lipodystrophies: From altered fat distribution to cellular alterations. *Biochem. Soc. Trans.* 39:1752–1757. https://doi.org/10.1042/BST20110675

Böddeker, T.J., K.A. Rosowski, D. Berchtold, L. Emmanouilidis, Y. Han, F.H.T. Allain, R.W. Style, L. Pelkmans, and E.R. Dufresne. 2022. Non-specific adhesive forces between filaments and membraneless organelles. *Nat. Phys.* 18:571–578. https://doi.org/10.1038/s41567-022-01537-8

Brasaemle, D.L., and N.E. Wolins. 2006. Isolation of lipid droplets from cells by density gradient centrifugation. *Curr. Protoc. Cell Biol.* 72:3.15.11–13.15.13. https://doi.org/10.1002/0471143030.cb0315s29

Castoldi, A., L.B. Monteiro, N. van Teijlingen Bakker, D.E. Sanin, N. Rana, M. Corrado, A.M. Cameron, F. Hässler, M. Matsushita, G. Caputa, et al. 2020. Triacylglycerol synthesis enhances macrophage inflammatory function. *Nat. Commun.* 11:4107. https://doi.org/10.1038/s41467-020-17881-3

Chanput, W., J.J. Mes, and H.J. Wichers. 2014. THP-1 cell line: An in vitro cell model for immune modulation approach. *Int. Immunopharmacol.* 23:37–45. https://doi.org/10.1016/j.intimp.2014.08.002

Chen, N.Y., Y. Yang, T.A. Weston, J.N. Belling, P. Heizer, Y. Tu, P. Kim, L. Edillo, S.J. Jonas, P.S. Weiss, et al. 2019. An absence of lamin B1 in migrating neurons causes nuclear membrane ruptures and cell death. *Proc. Natl. Acad. Sci. USA.* 116:25870–25879. https://doi.org/10.1073/pnas.1917225116

Cho, S., M. Vashisth, A. Abbas, S. Majkut, K. Vogel, Y. Xia, I.L. Ivanovska, J. Irianto, M. Tewari, K. Zhu, et al. 2019. Mechanosensing by the lamina protects against nuclear rupture, DNA damage, and cell-cycle arrest. *Dev. Cell.* 49:920–935.e5. https://doi.org/10.1016/j.devcel.2019.04.020

Coste, B., J. Mathur, M. Schmidt, T.J. Earley, S. Ranade, M.J. Petrus, A.E. Dubin, and A. Patapoutian. 2010. Piezo1 and Piezo2 are essential components of distinct mechanically activated cation channels. *Science.* 330:55–60. https://doi.org/10.1126/science.1193270

Cruz, A.L.S., E.A. Barreto, N.P.B. Fazolini, J.P.B. Viola, and P.T. Bozza. 2020. Lipid droplets: Platforms with multiple functions in cancer hallmarks. *Cell Death Dis.* 11:105. https://doi.org/10.1038/s41419-020-2297-3

De Vos, W.H., F. Houben, M. Kamps, A. Malhas, F. Verheyen, J. Cox, E.M.M. Manders, V.L. Verstraeten, M.A.M. van Steensel, C.L.M. Marcelis, et al. 2011. Repetitive disruptions of the nuclear envelope invoke temporary loss of cellular compartmentalization in laminopathies. *Hum. Mol. Genet.* 20:4175–4186. https://doi.org/10.1093/hmg/ddr344

Denais, C.M., R.M. Gilbert, P. Isermann, A.L. McGregor, M. te Lindert, B. Weigelin, P.M. Davidson, P. Friedl, K. Wolf, and J. Lammerding. 2016. Nuclear envelope rupture and repair during cancer cell migration. *Science.* 352:353–358. https://doi.org/10.1126/science.aad7297

Du, M., and Z.J.J. Chen. 2018. DNA-induced liquid phase condensation of cGAS activates innate immune signaling. *Science.* 361:704–709. https://doi.org/10.1126/science.aat1022

Farese, R.V., Jr, and T.C. Walther. 2009. Lipid droplets finally get a little R-E-S-P-E-C-T. *Cell.* 139:855–860. https://doi.org/10.1016/j.cell.2009.11.005

Gittes, F., B. Mickey, J. Nettleton, and J. Howard. 1993. Flexural rigidity of microtubules and actin filaments measured from thermal fluctuations in shape. *J. Cell Biol.* 120:923–934. https://doi.org/10.1083/jcb.120.4.923

Grundy, G.J., S.L. Rulten, Z. Zeng, R. Arribas-Bosacoma, N. Iles, K. Manley, A. Oliver, and K.W. Caldecott. 2013. APLF promotes the assembly and activity of non-homologous end joining protein complexes. *EMBO J.* 32: 112–125. https://doi.org/10.1038/emboj.2012.304

Harding, S.M., J.L. Benci, J. Irianto, D.E. Discher, A.J. Minn, and R.A. Greenberg. 2017. Mitotic progression following DNA damage enables pattern recognition within micronuclei. *Nature.* 548:466–470. https://doi.org/10.1038/nature23470

Hatch, E.M., A.H. Fischer, T.J. Deerinck, and M.W. Hetzer. 2013. Catastrophic nuclear envelope collapse in cancer cell micronuclei. *Cell.* 154:47–60. https://doi.org/10.1016/j.cell.2013.06.007

Heid, H., S. Rickelt, R. Zimbelmann, S. Winter, H. Schumacher, Y. Dörflinger, C. Kuhn, and W.W. Franke. 2014. On the formation of lipid droplets in human adipocytes: The organization of the perilipin-vimentin cortex. *PLoS One.* 9:e90386. https://doi.org/10.1371/journal.pone.0090386

Hill, D.A., H.W. Lim, Y.H. Kim, W.Y. Ho, Y.H. Foong, V.L. Nelson, H.C.B. Nguyen, K. Chegireddy, J. Kim, A. Habertheuer, et al. 2018. Distinct macrophage populations direct inflammatory versus physiological changes in adipose tissue. *Proc. Natl. Acad. Sci. USA.* 115:E5096–E5105. https://doi.org/10.1073/pnas.1802611115

Hotulainen, P., and P. Lappalainen. 2006. Stress fibers are generated by two distinct actin assembly mechanisms in motile cells. *J. Cell Biol.* 173: 383–394. https://doi.org/10.1083/jcb.200511093

Hsieh, K., Y.K. Lee, C. Londos, B.M. Raaka, K.T. Dalen, and A.R. Kimmel. 2012. Perilipin family members preferentially sequester to either triacylglycerol-specific or cholesteryl-ester-specific intracellular lipid storage droplets. *J. Cell Sci.* 125:4067–4076. https://doi.org/10.1242/jcs.104943

Irianto, J., C.R. Pfeifer, I.L. Ivanovska, J. Swift, and D.E. Discher. 2016. Nuclear lamins in cancer. *Cell. Mol. Bioeng.* 9:258–267. https://doi.org/10.1007/s12195-016-0437-8

Irianto, J., Y. Xia, C.R. Pfeifer, A. Athirasala, J. Ji, C. Alvey, M. Tewari, R.R. Bennett, S.M. Harding, A.J. Liu, et al. 2017. DNA damage follows repair factor depletion and portends genome variation in cancer cells after pore migration. *Curr. Biol.* 27:210–223. https://doi.org/10.1016/j.cub.2016.11.049

Israelachvili, J.N. 2011. Intermolecular and Surface Forces. Elsevier, Inc., Netherlands.

Ivanovska, I.L., J. Swift, K. Spinler, D. Dingal, S. Cho, and D.E. Discher. 2017. Cross-linked matrix rigidity and soluble retinoids synergize in nuclear lamina regulation of stem cell differentiation. *Mol. Biol. Cell.* 28: 2010–2022. https://doi.org/10.1091/mbc.e17-01-0010

Izumi, M., O.A. Vaughan, C.J. Hutchison, and D.M. Gilbert. 2000. Head and/or CaaX domain deletions of lamin proteins disrupt preformed lamin A and C but not lamin B structure in mammalian cells. *Mol. Biol. Cell.* 11: 4323–4337. https://doi.org/10.1091/mbc.11.12.4323

Kono, Y., S.A. Adam, Y. Sato, K.L. Reddy, Y. Zheng, O. Medalia, R.D. Goldman, H. Kimura, and T. Shimi. 2022. Nucleoplasmic lamin C rapidly accumulates at sites of nuclear envelope rupture with BAF and cGAS. *J. Cell Biol.* 221:e202201024. https://doi.org/10.1083/jcb.202201024

Lammerding, J., L.G. Fong, J.Y. Ji, K. Reue, C.L. Stewart, S.G. Young, and R.T. Lee. 2006. Lamins A and C but not lamin B1 regulate nuclear mechanics. *J. Biol. Chem.* 281:25768–25780. https://doi.org/10.1074/jbc.M513511200

Lomakin, A.J., C.J. Cattin, D. Cuvelier, Z. Alraies, M. Molina, G.P.F. Nader, N. Srivastava, P.J. Sáez, J.M. Garcia-Arcos, I.Y. Zhitnyak, et al. 2020. The nucleus acts as a ruler tailoring cell responses to spatial constraints. *Science.* 370:eaba2894. https://doi.org/10.1126/science.aba2894

Loneker, A.E., F. Alisafaei, A. Kant, D. Li, P.A. Janmey, V.B. Shenoy, and R.G. Wells. 2023. Lipid droplets are intracellular mechanical stressors that impair hepatocyte function. *Proc. Natl. Acad. Sci. USA.* 120:e2216811120. https://doi.org/10.1073/pnas.2216811120

Lyu, X., J. Wang, J. Wang, Y.S. Yin, Y. Zhu, L.L. Li, S. Huang, S. Peng, B. Xue, R. Liao, et al. 2021. A gel-like condensation of Cidec generates lipid-permeable plates for lipid droplet fusion. *Dev. Cell.* 56:2592–2606.e7. https://doi.org/10.1016/j.devcel.2021.08.015

Mannik, J., A. Meyers, and P. Dalhaimer. 2014. Isolation of cellular lipid droplets: Two purification techniques starting from yeast cells and human placentas. *J. Vis. Exp.* 86:50981

Mejhert, N., L. Kuruvilla, K.R. Gabriel, S.D. Elliott, M.A. Guie, H. Wang, Z.W. Lai, E.A. Lane, R. Christiano, N.N. Danial, et al. 2020. Partitioning of MLX-family transcription factors to lipid droplets regulates metabolic gene expression. *Mol. Cell.* 77:1251–1264.e9. https://doi.org/10.1016/j.molcel.2020.01.014

Mohseny, A.B., I. Machado, Y. Cai, K.L. Schaefer, M. Serra, P.C.W. Hogendoorn, A. Llombart-Bosch, and A.M. Cleton-Jansen. 2011. Functional characterization of osteosarcoma cell lines provides representative models to study the human disease. *Lab. Invest.* 91:1195–1205. https://doi.org/10.1038/labinvest.2011.72

Murphy, D.J., and J. Vance. 1999. Mechanisms of lipid-body formation. *Trends Biochem. Sci.* 24:109–115. https://doi.org/10.1016/S0968-0004(98)01349-8

Nieman, K.M., H.A. Kenny, C.V. Penicka, A. Ladanyi, R. Buell-Gutbrod, M.R. Zillhardt, I.L. Romero, M.S. Carey, G.B. Mills, G.S. Hotamisligil, et al. 2011. Adipocytes promote ovarian cancer metastasis and provide energy for rapid tumor growth. *Nat. Med.* 17:1498–1503. https://doi.org/10.1038/nm.2492

Nmezi, B., J. Xu, R. Fu, T.J. Armiger, G. Rodriguez-Bey, J.S. Powell, H. Ma, M. Sullivan, Y. Tu, N.Y. Chen, et al. 2019. Concentric organization of A- and B-type lamins predicts their distinct roles in the spatial organization and stability of the nuclear lamina. *Proc. Natl. Acad. Sci. USA.* 116: 4307–4315. https://doi.org/10.1073/pnas.1810070116

Olins, A.L., G. Rhodes, D.B.M. Welch, M. Zwerger, and D.E. Olins. 2010. Lamin B receptor: Multi-tasking at the nuclear envelope. *Nucleus.* 1: 53–70. https://doi.org/10.4161/nucl.1.1.10515

Pfeifer, C.R., M.P. Tobin, S. Cho, M. Vashisth, L.J. Dooling, L.L. Vazquez, E.G. Ricci-De Lucca, K.T. Simon, and D.E. Discher. 2022. Gaussian curvature dilutes the nuclear lamina, favoring nuclear rupture, especially at high strain rate. *Nucleus.* 13:129–143. https://doi.org/10.1080/19491034.2022.2045726

Pfeifer, C.R., Y. Xia, K. Zhu, D. Liu, J. Irianto, V.M.M. García, L.M.S. Millán, B. Niese, S. Harding, D. Deviri, et al. 2018. Constricted migration increases DNA damage and independently represses cell cycle. *Mol. Biol. Cell.* 29: 1948–1962. https://doi.org/10.1091/mbc.E18-02-0079

Pfisterer, S.G., G. Gateva, P. Horvath, J. Pirhonen, V.T. Salo, L. Karhinen, M. Varjosalo, S.J. Ryhänen, P. Lappalainen, and E. Ikonen. 2017. Role for formin-like 1-dependent acto-myosin assembly in lipid droplet dynamics and lipid storage. *Nat. Commun.* 8:14858. https://doi.org/10.1038/ncomms14858

Pontén, J., and E. Saksela. 1967. Two established in vitro cell lines from human mesenchymal tumours. *Int. J. Cancer.* 2:434–447. https://doi.org/10.1002/ijc.2910020505

Raab, M., M. Gentili, H. de Belly, H.R. Thiam, P. Vargas, A.J. Jimenez, F. Lautenschlaeger, R. Voituriez, A.M. Lennon-Duménil, N. Manel, and M. Piel. 2016. ESCRT III repairs nuclear envelope ruptures during cell migration to limit DNA damage and cell death. *Science.* 352:359–362. https://doi.org/10.1126/science.aad7611

Ralhan, I., C.L. Chang, J. Lippincott-Schwartz, and M.S. Ioannou. 2021. Lipid droplets in the nervous system. *J. Cell Biol.* 220:e202102136. https://doi.org/10.1083/jcb.202102136

Robijns, J., F. Molenberghs, T. Sieprath, T.D.J. Corne, M. Verschuuren, and W.H. De Vos. 2016. In silico synchronization reveals regulators of nuclear ruptures in lamin A/C deficient model cells. *Sci. Rep.* 6:30325. https://doi.org/10.1038/srep30325

Schott, M.B., S.G. Weller, R.J. Schulze, E.W. Krueger, K. Drizyte-Miller, C.A. Casey, and M.A. McNiven. 2019. Lipid droplet size directs lipolysis and lipophagy catabolism in hepatocytes. *J. Cell Biol.* 218:3320–3335. https://doi.org/10.1083/jcb.201803153

Shoham, N., P. Girshovitz, R. Katzengold, N.T. Shaked, D. Benayahu, and A. Gefen. 2014. Adipocyte stiffness increases with accumulation of lipid droplets. *Biophys. J.* 106:1421–1431. https://doi.org/10.1016/j.bpj.2014.01.045

Spiegelman, B.M., and S.R. Farmer. 1982. Decreases in tubulin and actin gene expression prior to morphological differentiation of 3T3 adipocytes. *Cell*. 29:53–60. https://doi.org/10.1016/0092-8674(82)90089-7

Su, P., Q. Wang, E. Bi, X. Ma, L. Liu, M. Yang, J. Qian, and Q. Yi. 2020. Enhanced lipid accumulation and metabolism are required for the differentiation and activation of tumor-associated macrophages. *Cancer Res.* 80:1438–1450. https://doi.org/10.1158/0008-5472.CAN-19-2994

Swift, J., I.L. Ivanovska, A. Buxboim, T. Harada, P.C. Dingal, J. Pinter, J.D. Pajerowski, K.R. Spinler, J.W. Shin, M. Tewari, et al. 2013. Nuclear lamin-A scales with tissue stiffness and enhances matrix-directed differentiation. *Science*. 341:1240104. https://doi.org/10.1126/science.1240104

Tamiello, C., M.A.F. Kamps, A. van den Wijngaard, V.L. Verstraeten, F.P.T. Baaijens, J.L.V. Broers, and C.C.V. Bouten. 2013. Soft substrates normalize nuclear morphology and prevent nuclear rupture in fibroblasts from a laminopathy patient with compound heterozygous LMNA mutations. *Nucleus*. 4:61–73. https://doi.org/10.4161/nucl.23388

Thiam, A.R., R.V. Farese Jr, and T.C. Walther. 2013. The biophysics and cell biology of lipid droplets. *Nat. Rev. Mol. Cell Biol.* 14:775–786. https://doi.org/10.1038/nrm3699

Tseng, L.C., and R.H. Chen. 2011. Temporal control of nuclear envelope assembly by phosphorylation of lamin B receptor. *Mol. Biol. Cell*. 22:3306–3317. https://doi.org/10.1091/mbc.e11-03-0199

Turgay, Y., M. Eibauer, A.E. Goldman, T. Shimi, M. Khayat, K. Ben-Harush, A. Dubrovsky-Gaupp, K.T. Sapra, R.D. Goldman, and O. Medalia. 2017. The molecular architecture of lamins in somatic cells. *Nature*. 543:261–264. https://doi.org/10.1038/nature21382

Valm, A.M., S. Cohen, W.R. Legant, J. Melunis, U. Hershberg, E. Wait, A.R. Cohen, M.W. Davidson, E. Betzig, and J. Lippincott-Schwartz. 2017. Applying systems-level spectral imaging and analysis to reveal the organelle interactome. *Nature*. 546:162–167. https://doi.org/10.1038/nature22369

Venturini, V., F. Pezzano, F. Català Castro, H.M. Häkkinen, S. Jiménez-Delgado, M. Colomer-Rosell, M. Marro, Q. Tolosa-Ramon, S. Paz-López, M.A. Valverde, et al. 2020. The nucleus measures shape changes for cellular proprioception to control dynamic cell behavior. *Science*. 370:eaba2644. https://doi.org/10.1126/science.aba2644

Verstraeten, V.L., J. Renes, F.C.S. Ramaekers, M. Kamps, H.J. Kuijpers, F. Verheyen, M. Wabitsch, P.M. Steijlen, M.A.M. van Steensel, and J.L.V. Broers. 2011. Reorganization of the nuclear lamina and cytoskeleton in adipogenesis. *Histochem. Cell Biol.* 135:251–261. https://doi.org/10.1007/s00418-011-0792-4

Welte, M.A. 2009. Fat on the move: Intracellular motion of lipid droplets. *Biochem. Soc. Trans.* 37:991–996. https://doi.org/10.1042/BST0370991

Xia, Y., I.L. Ivanovska, K. Zhu, L. Smith, J. Irianto, C.R. Pfeifer, C.M. Alvey, J. Ji, D. Liu, S. Cho, et al. 2018. Nuclear rupture at sites of high curvature compromises retention of DNA repair factors. *J. Cell Biol.* 217:3796–3808. https://doi.org/10.1083/jcb.201711161

Xia, Y., C.R. Pfeifer, K. Zhu, J. Irianto, D. Liu, K. Pannell, E.J. Chen, L.J. Dooling, M.P. Tobin, M. Wang, et al. 2019. Rescue of DNA damage after constricted migration reveals a mechano-regulated threshold for cell cycle. *J. Cell Biol.* 218:2545–2563. https://doi.org/10.1083/jcb.201811100

Yang, P., H. Qin, Y. Li, A. Xiao, E. Zheng, H. Zeng, C. Su, X. Luo, Q. Lu, M. Liao, et al. 2022. CD36-mediated metabolic crosstalk between tumor cells and macrophages affects liver metastasis. *Nat. Commun.* 13:5782. https://doi.org/10.1038/s41467-022-33349-y

Supplemental material

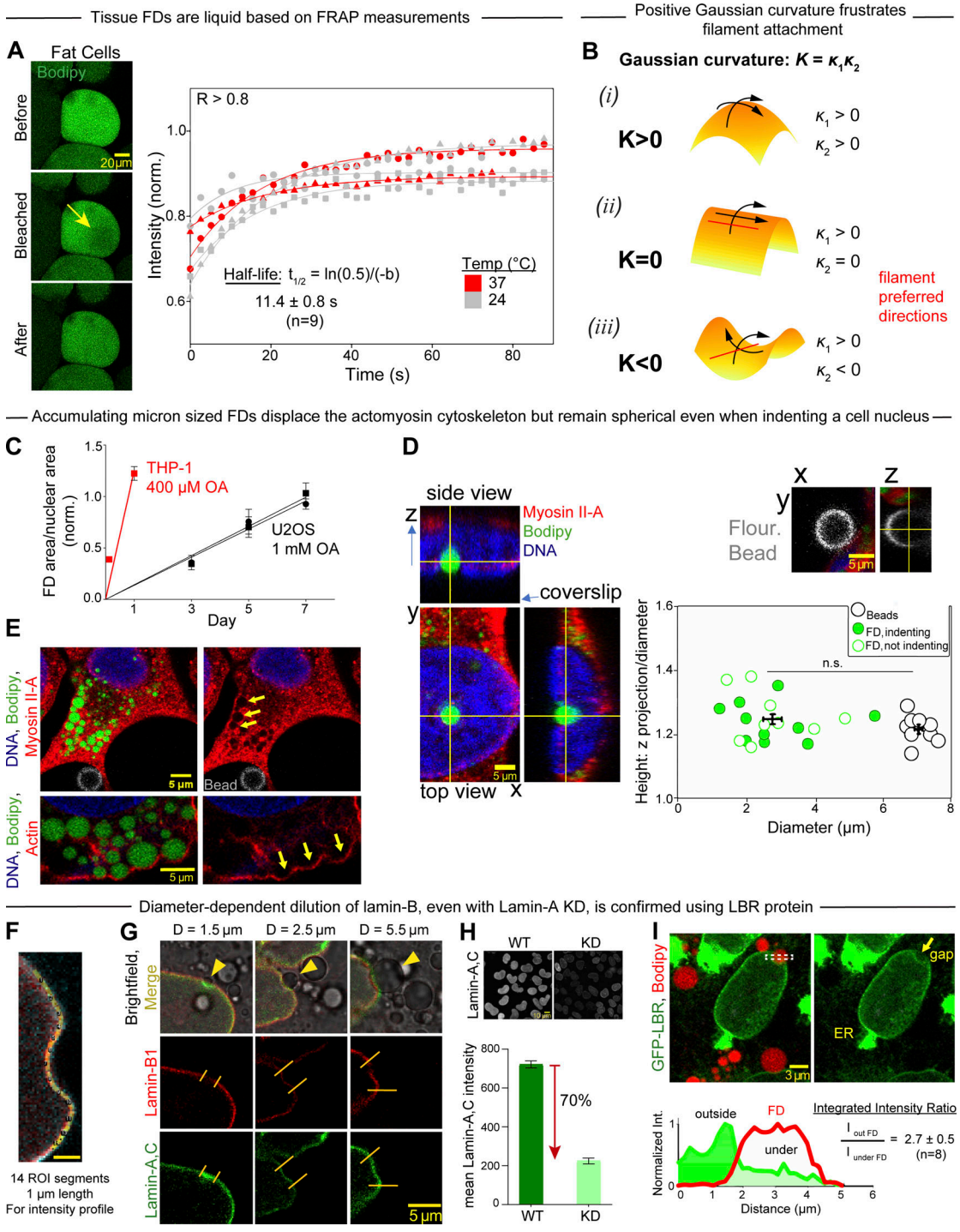

Figure S1. **FDs are liquid, are spherical when small, and indent actomyosin and the nuclear lamina. (A)** FDs within freshly isolated tissue show liquid-like mobility based on FRAP experiments that show a rapid recovery time across a range of temperatures (n = 5). **(B)** Positive Gaussian curvature is induced in the nuclear lamina by indenting FDs. For comparison, surfaces with zero Gaussian curvature and with negative Gaussian curvature allow attachment of rigid filament (red segment) in particular orientations. **(C)** Total area of FDs grows over time in a cell-type-dependent manner. A high concentration (1 mM) of oleic acid in U2OS fills an area equivalent to the nucleus size by day 7 (n = 1,600 cells, N = 2 experiments), whereas a lower oleic acid concentration (400 μM) fills the cytosol of THP-1 macrophages much more quickly (n = 50 cells, duplicate experiments). **(D)** Confocal z-stacks of U2OS cells confirm that FDs show no change in sphericity when indenting a cell nucleus, with a similar height: diameter ratio for indenting FDs, non-indenting FDs, and nondeformable silica beads (n = 19 FDs, n = 9 beads). **(E)** Cytoplasmic FDs displace or disrupt the organization of the U2OS cell's actomyosin meshwork, based on exclusion of myosin-IIA at FD sites as well as deformation of acto-myosin fibers (arrows). **(F)** Nuclear lamina intensity quantitation was done along 1 micron line segments in order to measure relative dilution within an indentation site as compared to adjacent regions. Scale bar = 1 μm. **(G)** Across a range of high curvature indentations by FDs (arrowheads), Lamin-B1 depletion is consistently observed in U2OS cells whereas Lamin-A,C varies from accumulation or no change to some depletion. **(H)** Lamin-A knockdown (KD) cells in U2OS cells showed a large decrease in mean intensity (~70%) relative to control cells. **(I)** LBR, a marker correlated with lamin-B level, is also depleted at FD-induced indentation sites in U2OS cells.

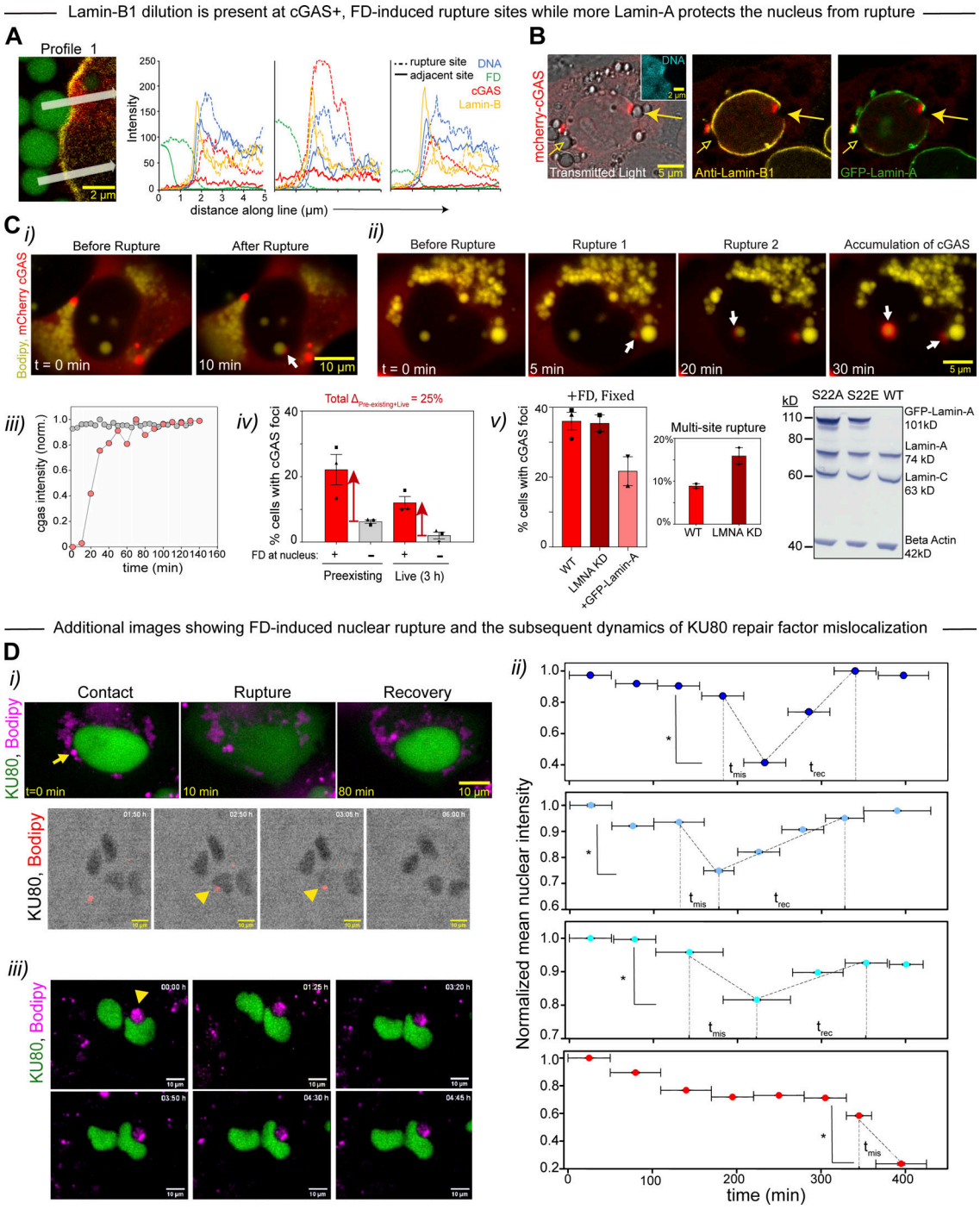

Figure S2. **Nuclear rupture by small FDs depends on lamin-A levels. (A)** Additional examples of FD-induced nuclear rupture with the FD colocalizing with Lamin-B1 depletion and accumulation of mCherry-cGAS. One line profile goes through the indentation-rupture site, and the second profile goes through the non-ruptured site. Line profiles show at rupture sites that both cGAS and DNA are more dense, whereas Lamin-B1 is depleted (n = 3 nuclei). **(B)** GFP-Lamin-A transduced U2OS cells show accumulation at a rupture site (arrow) but dilution at a non-rupture site of FD-indentation at the opposite pole; Lamin-B1 dilutes at both sites of FD-induced indentation (representative of n = 3 cells). **(C)** Additional live imaging examples of FD-induced nuclear rupture (per Fig. 2 A). **(C i)** After contact with an FD, the top of a nucleus is ruptured and begins to accumulate cGAS (arrow). **(C ii)** cGAS foci arise at two distinct nuclear sites within the same nucleus, and both foci appear at regions that are in close proximity to small diameter FDs (arrows). **(C iii)** Spatiotemporal kinetics of cGAS illustrates accumulation of cGAS around an FD contact site by 10 min that lasts for hours. **(C iv)** At the start of live imaging (t = 0) and during live imaging, nearly all rupture events show an FD in close proximity to a cGAS scar. **(C v)** Knockdown (KD) of Lamin-A (LMNA) showed increased multi-site rupture by FDs (duplicates, n = 200), whereas Lamin-A overexpression suppressed the frequency of nuclear rupture (duplicates, n = 120 cells). Immunoblot for Lamin-A,C indicates the overexpression level of GFP–Lamin-A in transduced U2OS relative to B-actin. **(D i)** Additional live imaging examples of KU80 mislocalization (per Fig. 2 C) after FD-nuclear contact (arrows or arrowheads) followed by slow recovery over 2–3 h. **(D ii)** Large FDs impose low curvature on the nucleus and do not trigger nuclear rupture with KU80 mislocalization, despite deep indentations. **(D iii)** Kinetics (20 min bins) of KU80 mislocalization for rupturing nuclei during live imaging (*, P < 0.05). Source data are available for this figure: SourceData FS2.

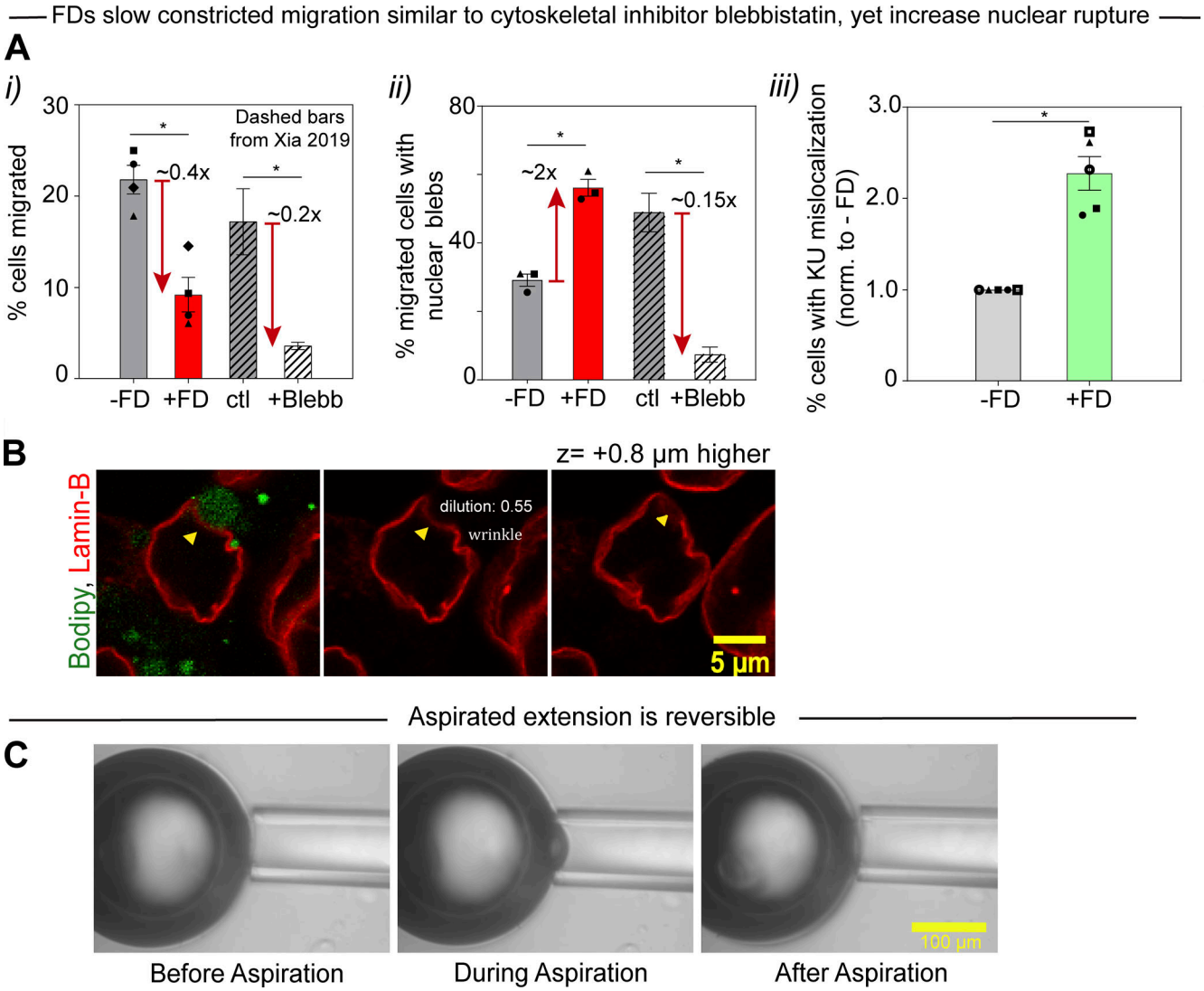

Figure S3. **FDs impede constricted migration, indent with Gaussian curvature, and deform reversibly. (A i)** Cytoskeleton-disrupting FDs reduce cell migration (Fig. 3, D ii) similar to the myosin-II inhibitor blebbistatin, which also suppresses migration through constricting pores. **(A ii)** However, blebbistatin reduces nuclear rupture after constricted migration, whereas FDs cause a twofold increase in nuclear rupture. **(A iii)** FDs cause more KU80 or KU70 mislocalization relative to control cells in both 2D cultures (open points; Fig. 2 D fixed and live) and 3D Transwell migration studies (filled points; Fig. 3, D iv). **(B)** Lamin-B1 dilution at sites of FD-driven Gaussian curvature remains visible across consecutive slices within a 1 µm z-space; the relative density of Lamin-B1 is 0.55 (day 2 after droplet induction). Nearby wrinkle lacks Gaussian curvature and does not show Lamin-B1 dilution even in the presence of an FD. **(C)** Isolated FDs show an elastic recovery when aspiration pressure is removed.